

## Determination of Mobile Ion Densities in Halide Perovskites via Low-Frequency Capacitance and Charge Extraction Techniques

Jonas Diekmann, Francisco Peña-Camargo, Nurlan Tokmoldin, Jarla Thiesbrummel, Jonathan Warby, Emilio Gutierrez-Partida, Sahil Shah, Dieter Neher, and Martin Stolterfoht\*



Cite This: *J. Phys. Chem. Lett.* 2023, 14, 4200–4210



Read Online

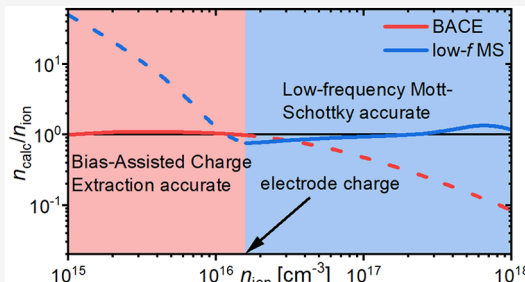
ACCESS |

Metrics & More

Article Recommendations

Supporting Information

**ABSTRACT:** Mobile ions in perovskite photovoltaic devices can hinder performance and cause degradation by impeding charge extraction and screening the internal field. Accurately quantifying mobile ion densities remains a challenge and is a highly debated topic. We assess the suitability of several experimental methodologies for determining mobile ion densities by using drift-diffusion simulations. We found that charge extraction by linearly increasing voltage (CELIV) underestimates ion density, but bias-assisted charge extraction (BACE) can accurately reproduce ionic lower than the electrode charge. A modified Mott–Schottky (MS) analysis at low frequencies can provide ion density values for high excess ionic densities, typical for perovskites. The most significant contribution to capacitance originates from the ionic depletion layer rather than the accumulation layer. Using low-frequency MS analysis, we also demonstrate light-induced generation of mobile ions. These methods enable accurate tracking of ionic densities during device aging and a deeper understanding of ionic losses.



To meet the increasing demand for renewable energies, much effort has been directed toward researching highly efficient and stable solar cells (SCs). One of the promising candidates for new solar materials is the class of metal halide perovskites. The perovskites' high absorption coefficient and reasonably long charge carrier lifetime have allowed single-junction perovskite solar cells (PSCs) to overcome power conversion efficiencies of 25% with thin films (~500 nm),<sup>1</sup> approaching the efficiency of monocrystalline silicon (26.7%).<sup>2</sup>

However, compared to traditional solar cell materials, perovskites are mixed ionic electronic semiconductors, a feature which significantly impacts the cell's characteristics. Mobile ions may migrate inside the device, screening the electric field in the bulk and lowering electronic drift currents.<sup>3</sup> Thus, ionic migration has been linked to losses in open-circuit-voltage ( $V_{oc}$ ),<sup>4</sup> short-circuit-current ( $J_{sc}$ ),<sup>5</sup> and fill factor (FF).<sup>6</sup> Another primary concern in PSCs is device stability<sup>7–10</sup> since PSCs need to reach a stability comparable to that of silicon SCs to be economically competitive and achieve the same levelized cost of electricity.<sup>11</sup> Most degradation processes have been attributed to mobile ions and may be induced by various external influences such as oxygen,<sup>12</sup> moisture,<sup>12</sup> illumination,<sup>13</sup> heat,<sup>14</sup> or lattice strain.<sup>15</sup> Furthermore, the ionic movement has been linked to the experimental observation of hysteresis,<sup>16,39,40</sup> halide segregation,<sup>17</sup> and dielectric screening.<sup>18</sup> Additionally, mobile ions alter the electroluminescence yield in perovskite light-emitting diodes and reduce their long-term stability.<sup>19</sup>

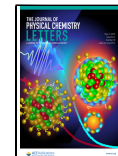
This selection highlights the significant impact of ionic migration on electrical characterization and solar cell performance. In order to understand and mitigate these effects, it is necessary to reliably characterize ion migration, specifically the density of mobile ions in perovskites. Although several different techniques such as charge extraction,<sup>5,20,21</sup> frequency-dependent capacitance,<sup>22,23</sup> transient capacitance,<sup>24</sup> galvanostatic polarization, Kelvin probe force microscopy,<sup>25,26</sup> and density functional theory<sup>27</sup> have been used to estimate ion density, there is no universally applicable technique for a large range of ion densities and no consensus has been reached yet on the reliability of the obtained results. For example, different techniques often result in very different ion densities (e.g., for MAPI the values range from  $10^{13} \text{ cm}^{-3}$  to  $10^{19} \text{ cm}^{-3}$ ).<sup>23,27</sup> Moreover, to our knowledge, there is no study where the applicability of the herein presented experimental techniques was corroborated by drift-diffusion simulations or where multiple techniques were used to confirm the obtained ion densities independently.

Two of the most extensively applied methods are charge extraction and capacitance measurements. The working

Received: February 24, 2023

Accepted: April 20, 2023

Published: April 28, 2023



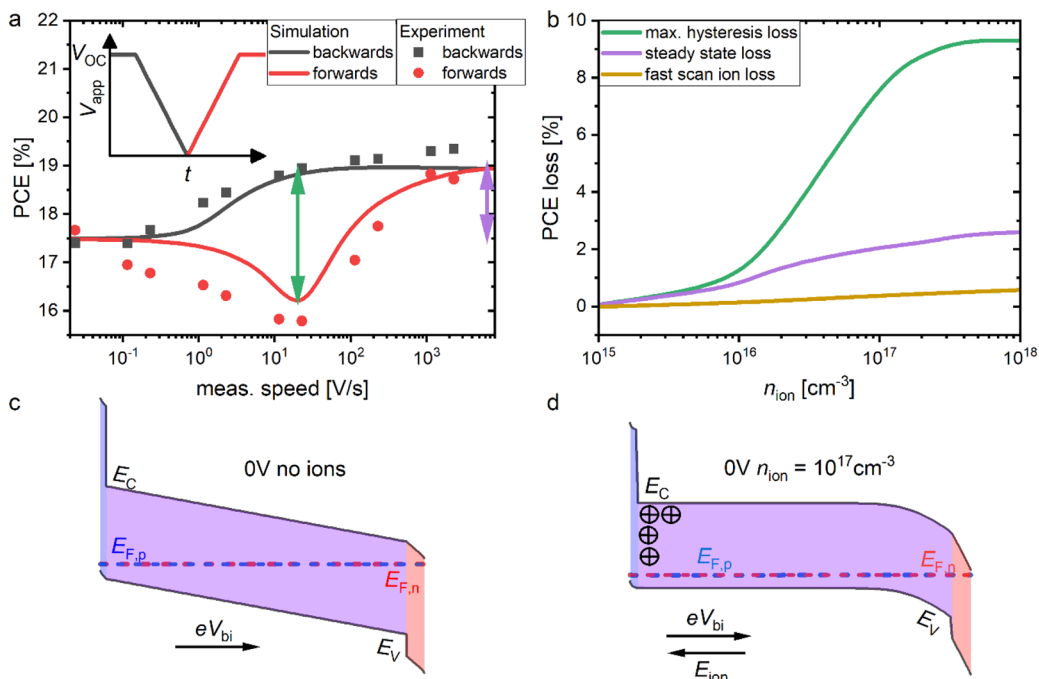


**Figure 1.** (a) Experimentally and numerically obtained JV-efficiencies for the backward and forward scan at various measurement speeds using our reference model with a mobile ion density of  $2 \times 10^{16} \text{ cm}^{-3}$ . The arrows indicate the relevant differences for panel b. PCE-losses caused by mobile ions as a function of mobile ion densities are determined from the PCE at the peak hysteresis (green), the difference between the PCE at fast and slow speeds (purple), and the difference between the PCE at very fast scan speeds and the PCE in absence of mobile ions (yellow). (c) Band diagram of the reference cell at 0 V shows a linear field drop across the device. (d) Implementing mobile cations leads to field screening in the bulk and on the HTL side, which reduces drift and impedes charge extraction. We note the remaining anions are fixed throughout the whole active layer.

principle of charge extraction measurements is to alter the applied field, leading to a redistribution of mobile ions. The displacement current produced from this movement can be integrated to obtain the mobile ion density. For example, in the case of charge extraction by linearly increasing voltage measurements (CELIV), the ions are driven by a linearly increasing field, while BACE is based on suddenly switching from a preconditioning to an extraction voltage. Bertolluzzi et al. developed a more evolved extraction method to measure ion density which is based on an analytical approach and multiple voltage steps.<sup>28</sup> The mentioned charge extraction methods revealed ion densities from  $1.5 \times 10^{16} \text{ cm}^{-3}$  to  $4 \times 10^{17} \text{ cm}^{-3}$  for commonly used perovskites.<sup>5,20,21</sup>

In the case of capacitance measurements, typically the low-frequency capacitance of the device is attributed to mobile ions, since they are significantly slower than electrons or holes. This capacitance is thought to originate from the formation of a space charge layer by the mobile ions, which allows equating the measured capacitance or the change thereof to a parallel plate capacitor where the plate distance is equal to the Debye length.<sup>22</sup> In contrast, Futscher et al. and others used transient capacitance or deep-level transient spectroscopy (DLTS) to compute the ionic density by relating the change in capacitance to the ratio between the mobile ion and the doping density using an estimated doping density of  $10^{17} \text{ cm}^{-3}$ .<sup>24</sup> However, various recent works have shown that the doping density of typical Pb-based perovskites ( $10^{11}$ – $10^{13} \text{ cm}^{-3}$ ) is too low to influence the internal field distribution based on various experimental techniques including photo Hall effect.<sup>29,30</sup> On the other hand, Fischer et al. employed high-frequency C–V-measurements after a forward voltage prebias and obtained ion densities of  $2.8 \times 10^{16} \text{ cm}^{-3}$  for MAPI.<sup>31</sup>

Generally, using capacitive techniques produces a broader range of ion densities from  $10^{13} \text{ cm}^{-3}$  to  $2.4 \times 10^{17} \text{ cm}^{-3}$  for MAPI.<sup>22,23</sup>

In this work, we aim to understand how to accurately determine the ion density in organic metal-halide perovskites devices based on various experimental methodologies. We evaluate different types of measurements, which were conducted on a standard triple cation PSC, based on their ability to reproduce input ion densities with numerical simulations accurately. To achieve this, we first establish a numerical model in the drift-diffusion simulator SETFOS that can reproduce the observed ionic effects and losses in current–voltage measurements. Furthermore, we confirm that field screening caused by ionic accumulation is responsible for hysteresis and steady-state operating losses. Using this model, we evaluate the CELIV method and find that it is rather unsuitable for accurately determining ion densities due to the inhomogeneous initial ion distribution and the necessary long measurement times. In contrast, BACE can accurately reproduce mobile ion densities by integrating the current over the ion-dominated regime. However, this only applies if the total ionic charge is lower than the CV-charge on the electrodes because the field-screening effect at higher ion densities prevents further redistribution of mobile ions. Additionally, we perform simulations of frequency-dependent capacitance. We show that the results can be modeled as a series of R||C-circuits, as is evident from the potential distribution in the perovskite. We find that the cation depletion layer, not the accumulation layer, displays the largest field drop and capacitance. Consequently, the commonly used Debye layer approximation severely underestimates the ionic density, while using the depletion layer approximation yields correct

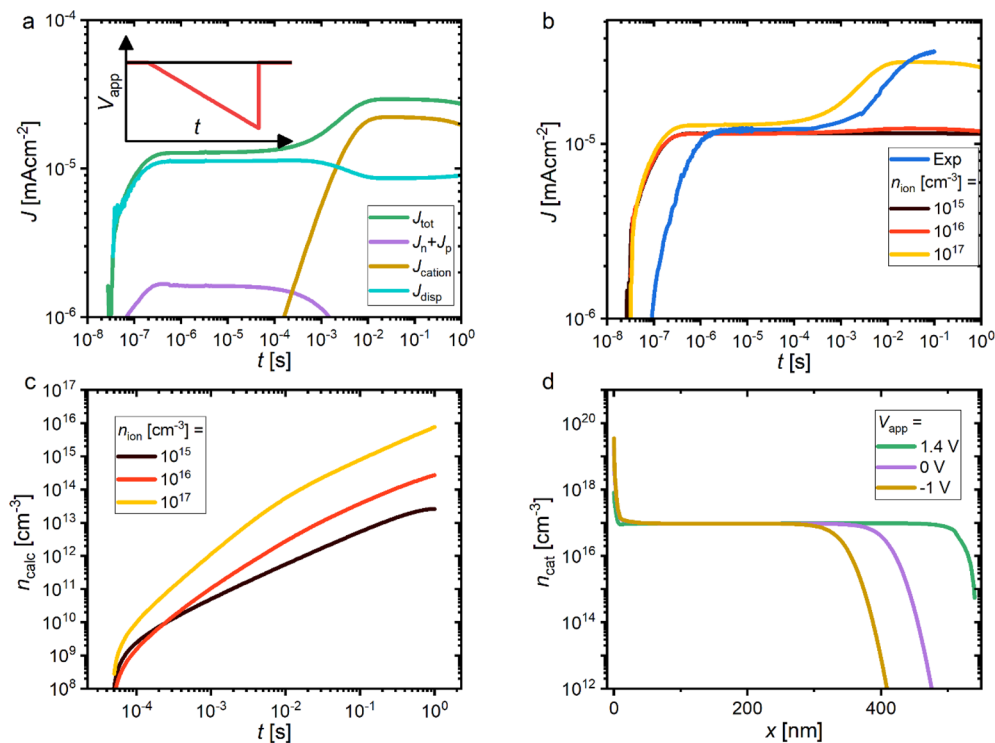


**Figure 2.** (a) Simulated partial currents for the CELIV method with  $n_{ion} = 10^{17} \text{ cm}^{-3}$ . Initially, the displacement current due to capacitive discharge dominates, while ionic current produces a bump starting at  $\sim 1$  ms. (b) Experimental and simulated CELIV transients for various ion densities show that the ionic bump is larger at higher ionic densities. The experimental CELIV transient is constructed by measuring at various ramp times.<sup>34</sup> (c) Integrated simulated CELIV transients for various ion densities yield significantly lower ionic densities than what was put in. (d) Cation density prior to the measurement at different prebiases demonstrating the accumulation of vacancies toward the HTL side of the device. This limits the ionic charge that can be accessed by the measurement.

results if the ionic density is larger than the CV-charge. However, introducing transport layers (TLs) distorts the field drop and the capacitance. We show that in this case the Mott–Schottky analysis can be used at low frequencies to circumvent this by removing the dependence on the internal field distribution in the layer stack. Using this novel method allows us to accurately determine the mobile ion density above the CV-charge by measuring the low-frequency capacitance of the whole device stack at various applied voltages and calculating the resulting slope.

In order to investigate the influence of mobile ions in various measurement techniques, we aim to establish an accurate simulation model of a perovskite solar cell. Without loss of generality, we choose a triple cation cell with the following architecture as our reference cell: ITO/PTAA/PFN-Br/perovskite/C<sub>60</sub>/BCP/Cu, where ITO is indium tin oxide, PTAA is poly[bis(4-phenyl)(2,4,6-trimethylphenyl)amine], PFN-Br is Poly{9,9-bis[30-(*N,N*-dimethyl)-N-ethylammonium]-propyl}-2,7-fluorene}-alt-2,7-{9,9-di-n-octylfluorene} dibromide, and BCP is bathocuproine.<sup>32</sup> The model is based on previous studies, where we thoroughly verified the electrical parameters by comparing the simulation to a wide range of measurements, including the dark and light JV, the intensity-dependent  $V_{OC}$ , the recombination currents at  $V_{OC}$  as obtained from steady-state photoluminescence measurements, and a range of experimental JV of devices with different hole transport layers.<sup>33</sup> We then implement these parameters (Supplementary Table S1) into the drift-diffusion software SETFOS from Fluxim (Supplementary Note S1), which allows us to include mobile ions in our simulations. This inclusion

allows us to recreate the JV-hysteresis observed in our cells over a wide range of scan speeds ( $10^{-2}$ – $10^4$  V/s), as shown in Figure 1a for a fresh cell. While degradation may significantly alter the hysteresis curve, FH yields stable results as shown in Supplementary Figure S3. In the following, we denote the scan-rate-dependent JV measurement as “fast hysteresis” (FH) measurement.<sup>34</sup> Furthermore, we verify that losses in the performance characteristics of  $J_{SC}$ ,  $V_{OC}$ , and FF can be recreated (Supplementary Figure S4). In both simulation and experiment, the slow measurement yields lower PCEs than the high-scan speed measurement. Whereas the backward-scan PCE increases monotonously, the forward-scan PCE has a minimum at  $\sim 10$  V/s. This behavior can be explained by examining the ionic distribution at various voltage points and measurement speeds (Supplementary Figure S5). To achieve the experimentally observed hysteresis, we use a mobile cation density of  $2 \times 10^{16} \text{ cm}^{-3}$  and the same amount of immobile anions to retain charge neutrality. This density value fits within the broad range of densities from  $10^{15}$  to  $10^{18} \text{ cm}^{-3}$  predicted by various methods.<sup>5,20–22,35</sup> To fit the peak hysteresis, we use an ion diffusion constant  $D = 10^{-9} \text{ cm}^2/\text{s}$ , which corresponds to a mobility of  $\mu = 4 \times 10^{-8} \text{ cm}^2/(\text{V s})$ . This mobility value fits with previously reported values for iodine mobility in perovskites of  $2 \times 10^{-8} \text{ cm}^2/(\text{V s})$  to  $10^{-6} \text{ cm}^2/(\text{V s})$ .<sup>24,28,34,36–38</sup> We note that the scan time at the peak hysteresis has previously been linked to the transit time through the active layer,<sup>34</sup> although certain material and device parameters may cause a deviation from this agreement.<sup>3</sup> Moreover, we note that the magnitude of the hysteresis and ionic losses depends on various material and device-related

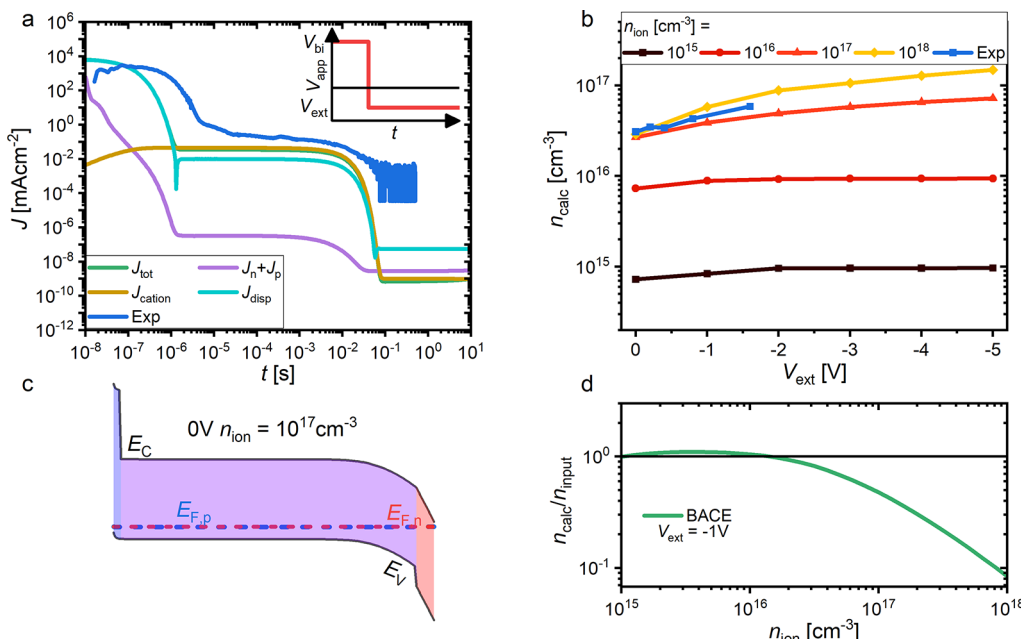


**Figure 3.** (a) Simulated partial currents for the BACE method with  $n_{\text{ion}} = 10^{17}$  cm<sup>-3</sup>. The ionic current produces a current plateau from 1  $\mu$ s to 10 ms. The experimental data is shown by the blue line. Notably, the ionic time-of-flight time (15 ms) matches roughly with the scan time in the fast-hysteresis measurement (Figure 1a). (b) Calculated ionic densities acquired by integrating the ionic current plateau from BACE simulations. Low ion densities saturate at low extraction voltages consistent with the input density. (c) The band diagram with an ionic density of  $10^{17}$  cm<sup>-3</sup> reveals the ion's field screening effect that prevents the measurement of a significant fraction of charges in the case of high ionic densities ( $>10^{16}$  cm<sup>-3</sup>) due to the consequent reduction in drift current. (d) Calculated ionic densities from BACE simulation as a function of the input ion density, using an extraction voltage of  $-1$  V. The calculated values show agreement with the input densities up to the electrode charge ( $10^{16}$  cm<sup>-3</sup>).

parameters. Overall, the FH measurement cannot be used to precisely quantify the ion density, which requires other experimental methodologies and forms the basis of this work.

Figure 1b shows that the observed losses are related to mobile ions since no losses are observed when the ion density is too low. Also, nearly no ionic losses are observed at high measurement speeds ( $>10^3$  V/s) because the ions are too slow to react to the changing field. Mobile ions cause these losses by redistributing the built-in voltage ( $V_{\text{bi}}$ ) in the absorber layer,<sup>18</sup> as demonstrated in the comparison of the band diagrams with and without mobile ions (Figure 1c,d), respectively. For the presented case of mobile ions, this screening creates a zero-field region in the active layer, increasing bulk recombination and reducing the field on the HTL-side, which impedes hole extraction current and increases interface recombination via an increased electron concentration next to the HTL (Supplementary Figure S6). The ion-induced increase of bulk and interface losses further underline the need for a reliable and coherent way of characterizing mobile ion density, which we will pursue in the following by assessing various measurement techniques.

The first method to determine mobile ion density which we will analyze is CELIV, which has been successfully used to quantify doping densities in organic semiconductors<sup>41</sup> and was recently applied in perovskite solar cells.<sup>5,34</sup> Herein, the device is kept in thermal equilibrium at 0 V, and the current transient is measured as the extraction (reverse bias) voltage increases linearly. The current transients are recorded by varying the slope as shown in previous work.<sup>34</sup> This measurement corresponds to charging a capacitor, where the cell acts as a dielectric material, resulting in a step function in current because the circuit differentiates the applied constant voltage gradient in the case of a small load resistances (e.g.,  $R_{\text{Load}} = 50$

Ohm).<sup>42</sup> Since our device has a finite series resistance and associated resistance–capacitance (RC) time constant, the resulting rise of the displacement current is not a step function, as shown in Figure 2a. Furthermore, since the device is not illuminated, the extracted electron and hole currents  $J_n$  and  $J_p$  can be neglected. Starting at the ms time scales, we observe a second bump in current due to the mobile ion movement that originates from the transport of ions to the respective electrodes in reverse bias, as evidenced by the steep rise of  $J_{\text{cation}}$  and its dominance over the displacement current for  $t > 1$  ms. As noted in previous works about charge extraction,<sup>34,43</sup> the ionic current does not originate from the ions being extracted through the electrodes from the solar cell. Rather, the ion's redistribution causes a change to the internal electric field which results in a displacement current equal to the ion current according to Maxwell's fourth equation. Another way to rationalize this behavior is that charges must flow through the external circuit when the ionic redistribution screens the internal field in order to maintain the potential difference between the two electrodes. The delayed response of the ions corresponds to their lower mobility (Supplementary Figure S7a).

Figure 2b shows that the magnitude of the second bump is indeed related to the ionic density, because no visible bump occurs at  $n_{\text{ion}} = 10^{15}$  cm<sup>-3</sup>. Higher ionic densities will yield higher and longer extraction currents. Also, the displacement current ( $J_{\text{displ}}$ ) decreases slightly at the onset of visible ion motion on the ms time scales, which is due to interaction between ionic and electronic conduction in the perovskite. However, the change is small compared to the ionic current. Therefore, we can calculate the ionic density by subtracting the baseline displacement from the current transient and integrating the remainder over time. The resulting integrated

transients reveal that the calculated ion density is significantly smaller than the input ion density (Figure 2c). The integral does not converge for high ionic densities since the current after 1 s is still larger than the displacement current. One could increase the measurement duration to alleviate this problem. However, this would decrease the voltage ramp rate ( $A$ ), which is proportional to the current ( $J = AC_{\text{geom}}$ , where  $C_{\text{geom}}$  is the geometrical capacitance per unit area). Measuring these low currents is hard to achieve experimentally and makes the method prone to errors. Even in the simulations, lowering the ramp rate does not enable resolving the whole bump (Supplementary Figure S8). In principle, increasing the reverse bias voltage would be the next logical step, but this could damage the sample. Also, for the case of two mobile ion species with opposite charge, CELIV is sensitive to the excess density of only one of the ionic species. This leads to the disappearance of the ionic bump for oppositely charged mobile ions with the same density that is shown in Supplementary Figure S9b.

Regardless of these problems, the calculated ionic density is underestimated even at low ion densities of  $10^{15} \text{ cm}^{-3}$ , where the integral still converges. This is because the internal built-in field at 0 V leads to an ionic accumulation close to the contact prior to the measurement (Figure 2d). Therefore, significant amounts of mobile ions have already moved and these do not contribute to the extraction current (discussed in detail further below). All in all, conventional CELIV with a 0 V prebias may be used to obtain a lower limit to the mobile ion density, but the initial ion distribution during the prebias and the long measurement times make it unsuitable for determining the ion density accurately. Some of these issues may be solved by prebiasing the cell at  $V_{\text{bi}}$ ; however, as discussed in Supplementary Figure S10, this leads essentially to a BACE transient, making the voltage ramp unnecessary.

Another widely used method to obtain mobile ion densities is BACE. In contrast to CELIV, the cell is kept at 1-sun- $V_{\text{OC}}$  (or if known  $V_{\text{bi}}$ ) prior to the measurement. The voltage is then switched to the extraction voltage, resulting in a discharge current with the  $RC$ -constant in the simulated case with  $R_{\text{series}} = 50 \Omega$ . For lower series resistances, the charge carrier mobility in one of the stack layers might be limiting the extraction. Figure 3a shows that the displacement current dominates initially before being overtaken by the ionic current, which is almost equal to the total current in the constant current regime from 1  $\mu\text{s}$  to 10 ms. Further current is added to the ionic current plateau when introducing mobile anions to the simulation, as shown in Supplementary Figure S9a. The current declines when the ions have reached a steady-state distribution close to the contacts at the respective extraction voltage. Interestingly, the transient is reminiscent of a time-of-flight (TOF) transient used for determining electronic charge transport in organic solar cells, however, in this case for ions. We note the calculated mobility from the “ion-TOF” is  $\mu = 1.4 \times 10^{-7} \text{ cm}^2/(\text{V s})$ , which matches the mobility obtained from the fast-hysteresis data ( $\mu = 10^{-7} \text{ cm}^2/(\text{V s})$ ) well. As shown in Supplementary Figure S7b, increasing the ionic mobility leads to shorter transient times. This technique has also been used in  $\sim 1 \text{ mm}$  thick perovskite pellets, obtaining an ion mobility of  $10^{-6} \text{ cm}^2/(\text{V s})$  to  $10^{-7} \text{ cm}^2/(\text{V s})$ .<sup>38</sup> We can then calculate the ion density by integrating the current in the ion-dominated regime

$$n_{\text{ion}} = \frac{d/d_{\text{drift}} \int J(t) dt}{de} \quad (1)$$

where  $e$  is the elementary charge,  $d$  the film thickness,  $d_{\text{drift}}$  the average drift length of carriers, and  $d/d_{\text{drift}}$  the geometric factor as described by Kniepert et al.<sup>44</sup> In the case of a homogeneous distribution of 1 mobile ion species (here positively charged halide vacancies) at the initial prebias condition, carriers will drift on average only half of the film thickness, thus  $d/d_{\text{drift}} = 2$  (this scenario is the case in our simulations). In the case of two mobile species and a homogeneous initial carrier distribution  $d/d_{\text{drift}} = 1$ . However, a higher factor ( $d/d_{\text{drift}}$ ) needs to be taken into account if carriers accumulate near the extracting contacts under the prebias (i.e., electrons at the cathode and hole at the anode), which results in shorter average drift lengths  $d_{\text{drift}}$ . This happens if the  $V_{\text{bi}}$  is not offset by the prebias and is among the reasons why conventional CELIV (prebias 0 V) generally underestimates the ion density, even for low input densities. In the BACE simulations, for one carrier type and applying approximately the  $V_{\text{bi}}$  as prebias, extracting at short-circuit condition yields a good approximation for low input ion densities of  $< 10^{16} \text{ cm}^{-3}$  (Figure 3b). Also, the calculated density values saturate at extraction voltages of  $-1 \text{ V}$ . Contrary to this, BACE severely underestimates higher ion densities, even when high extraction voltages are employed. This is because the ion’s field screening effect (Figure 3c) prevents additional ionic drift toward the HTL side after the initial redistribution. This effect becomes relevant only when the ionic charge is significantly larger than the charge on the electrodes. Accordingly, BACE is not accurate for the determination of ionic densities if

$$n_{\text{ion}} > n_{\text{electrode}} = \frac{C(V_{\text{bi}} - V_{\text{ext}})}{ed} \quad (2)$$

where  $C = \epsilon\epsilon_0 d^{-1} = 3 \times 10^{-8} \text{ F cm}^{-2}$  is the geometric capacitance per unit area and  $d = 500 \text{ nm}$  is the perovskite thickness. Consequently, using a realistic extraction voltage of  $-1 \text{ V}$ , which equates to an electrode charge density of  $\sim 10^{16} \text{ cm}^{-3}$ , the ionic density may be determined up to this threshold, as Figure 3d shows. We note that Fischer et al. also identified a very similar value as the upper limit for accurately measurable ionic densities in photovoltaic decay measurements.<sup>45</sup> Considering the similarities in device structure, this indicates that the limit given in eq 2 extends to other measurement methods. However, we note that higher ionic densities might be detectable in the experiment with BACE if the ions are extracted to the external circuit or if the ionic drift current is compensated by electrical charges which are not taken into account in the simulations. Nevertheless, in order to assess if the obtained ion density is smaller or larger than the electrode charge one may vary the extraction voltage (if no significant shunt is introduced). If the calculated charge saturates, field screening does not affect the result and the measured ion density is correct despite a small uncertainty concerning the initial distribution, as discussed above. This is however not the case in our cells, as shown in Figure 3b, suggesting that the ionic density is larger than the CV-charge. Lastly, from an experimental perspective it is noteworthy that the measurement of low ionic currents in the nA regime requires the use of a current meter rather than an oscilloscope which has (also depending on  $R_{\text{Load}}$ ) a much lower current resolution.

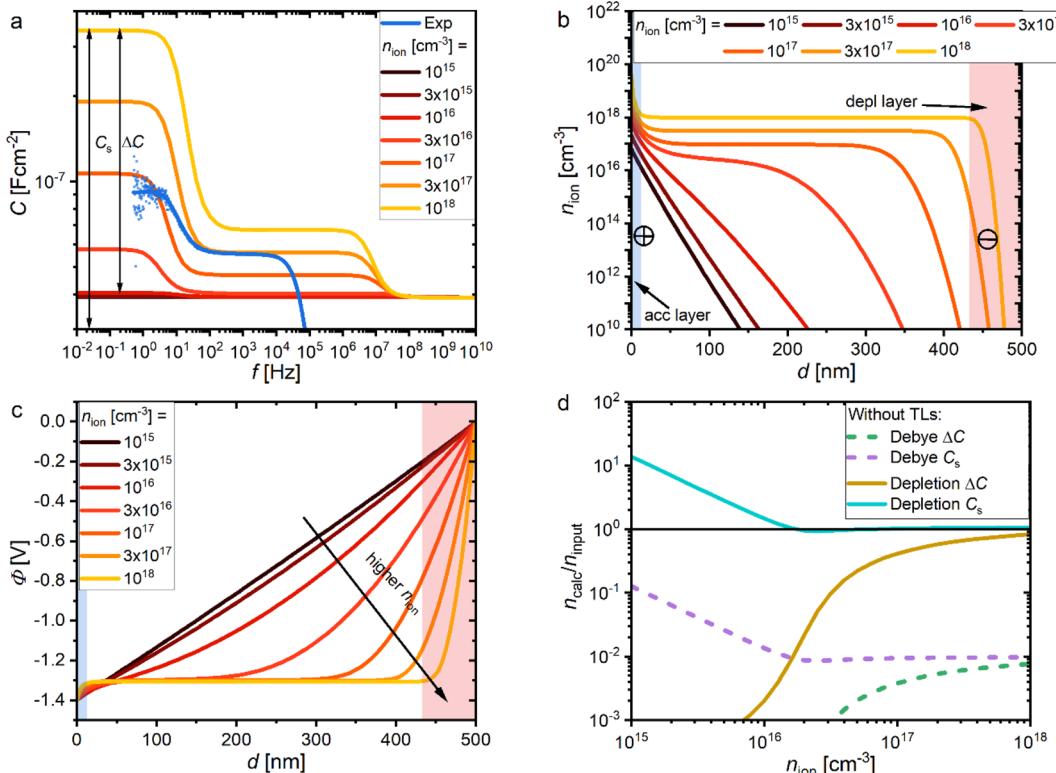


**Figure 4.** (a) Simulated capacitance vs frequency ( $C-f$ ) without transport layers showing three distinct capacitance plateaus for high ionic densities. The capacitance plateaus result from the frequency-dependent behavior of the capacitive reactance changing the dominant contribution as discussed in [Supplementary Note S2](#). (b) Ionic distribution at 0 V across the perovskite reveals the formation of an accumulation and a depletion layer for ionic densities higher than the electrode charge ( $>10^{16} \text{ cm}^{-3}$ ). (c) Potential drops over the perovskite for different ion densities. The ion accumulation results in three layers with different voltage drops which can each be modeled as plate capacitors connected in parallel to resistors. (d) Comparison of calculated to input ionic density for various capacitance analysis methods. While the Debye approximation underestimates the ionic density, the depletion layer equation (eq 4) is suitable for ionic densities larger than the electrode charge if no transport layers are employed, and the total capacitance at low frequencies is used.

Besides charge extraction measurements, impedance spectroscopy is used to approximate the mobile ion density in PSCs. Herein, the impedance ( $Z$ ) of the cell is measured at various frequencies, which yields the capacitance through calculation from the capacitive reactance ( $X$ ), i.e.

$$Z = R + X = R + \frac{1}{i\omega C} \quad (3)$$

where  $R$  is the series/load resistance and  $\omega$  is the angular frequency. As [Figure 4a](#) shows  $C$  for a cell without series resistance and TLs, the capacitance at high frequencies is the same for each ion density. The corresponding Nyquist plots are shown in [Supplementary Figure S11](#). Note that the experimental capacitance in the high-frequency regime is lowered by the series resistance, which is omitted in the simulations of [Figure 4a](#) ([Supplementary Figure S12](#)). Lowering the frequency increases the capacitance for high enough ionic densities in a step-like manner. The reason for this behavior can be deduced from [Figure 4b](#). The cations will migrate from the ETL-side (right) to the HTL-side (left) at short-circuit conditions. Assuming an initially neutral lattice,<sup>30</sup> this migration will result in the formation of a cation depletion layer at the right side and an ion accumulation layer at the left side, while the bulk will stay field-free for ion densities larger than the CV-charge, as shown in [Figure 4c](#). We note that the height of the capacitance step is sensitive to the excess of one mobile ionic charge only. This means that the capacitance

decreases in case of 2 mobile ion species with opposite sign as shown in [Supplementary Figure S13](#). While this needs to be taken into account for the analysis capacitance measurements, we note that halide vacancy transport is considered to dominate over interstitial transport because of their low activation energy,<sup>18,46</sup> while interstitial transport is inhibited by the close-packed nature of the perovskite.<sup>47</sup> Experimentally, this was confirmed by the observation of a decrease in ionic conductivity at higher iodine partial pressure<sup>36</sup> and the suppression of mobile-ion-related features in transient absorption spectroscopy upon the addition of excess iodine.<sup>48</sup> Therefore, we exemplify the results for halide vacancies only without ruling out the possibility of 2 equally dominant mobile species.

Ravishankar et al. developed a multilayer model based on a series connection of three  $R||C$ -circuits to describe the step-like behavior of capacitance.<sup>49</sup> In [Supplementary Note S2](#), we apply this model to our case. This reveals that the high-frequency capacitance equals the geometric capacitance, while the intermediate- and low-frequency capacitance can be attributed to electrostatic layers caused by holes and mobile ions, respectively. Although several previous studies have linked the low-frequency capacitance to mobile ions, it is unclear at this point how to obtain the ionic density from this value. First, one needs to decide whether the total capacitance value  $C_s$  or the difference to the high-frequency capacitance  $\Delta C$  is relevant. Additionally, two equations could be considered for the

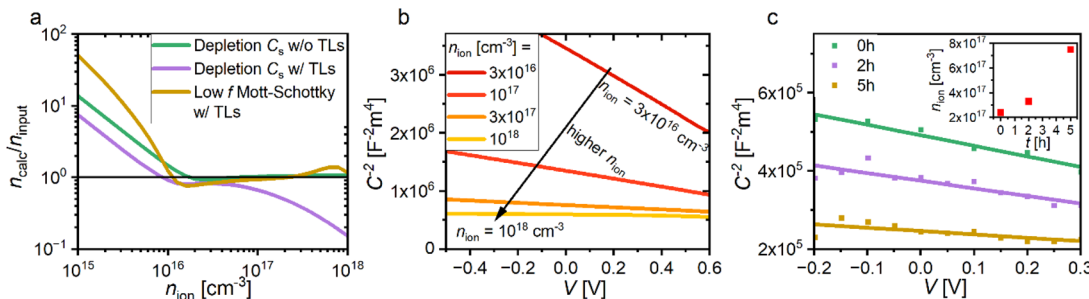


**Figure 5.** (a) Comparison of calculated to input ionic density for various capacitance analysis methods. Introducing transport layers (TLs) introduces a field drop across the TLs and distorts the obtained ionic density from the depletion layer equation (eq 5). Low-frequency Mott–Schottky analysis (eq 6) can accurately recover the input ion density for high ionic densities, even with TLs. (b) Mott–Schottky analysis at low frequency ( $f = 5 \text{ Hz}$ ) reveals the expected linear dependence on voltage. Increasing ion density results in lower slopes. (c) Experimentally acquired low-frequency (5 Hz) Mott–Schottky curves for different aging times under 1 sun equivalent illumination and open-circuit conditions obtained in ambient atmosphere on encapsulated devices. Calculating the ionic density from the respective slopes reveals a light-induced generation of mobile ions over the aging time.

capacitance of an electrostatic layer. The first one is the equation for the capacitance of a Debye (accumulation) layer<sup>23</sup>

$$C_{\text{acc}}^2 = \frac{n_{\text{ion}} e \epsilon \epsilon_0}{V_{\text{th}}} \quad (4)$$

where  $V_{\text{th}} = \frac{kT}{e}$  is the thermal voltage. The second possibility is the capacitance of a depletion layer

$$C_{\text{depl}}^2 = \frac{n_{\text{ion}} e \epsilon \epsilon_0}{2(V_{\text{th}} + V_{\text{bi}} - V_{\text{app}})} \quad (5)$$

The difference between these two equations is the effective voltage  $V_{\text{bi}} - V_{\text{app}}$  across the depletion layer, which defines the depletion region in case of high ion densities, while  $eV < kT$  is presumed in the Debye layer equation. To know whether we are probing an accumulation or a depletion layer and whether the high-frequency capacitance should be subtracted, we compare the input ionic density to the calculated one for all four combinations. For the sake of simplification, we first omit TLs. Figure 4d shows that the Debye equation yields values that are significantly lower than the input. In contrast to this, the depletion layer equation using the total capacitance (purple line) reveals a good agreement with the input values if  $n_{\text{ion}} > \frac{CV_{\text{bi}}}{de}$ . This critical measurement level is due to the competition of the amount of charge inside the active layer versus the electrode charge or equivalently due to the relation between the depletion width and the device thickness, as Ravishankar et al. recently discussed.<sup>50</sup> They also find an analytical resolution limit that is a variant of the CV-limit presented herein.<sup>51</sup> Using  $\Delta C$ , the obtained values converge eventually. However, this is only coincidental since the high-frequency capacitance becomes negligible compared to  $C_s$  at high ionic densities. We can thus conclude that the low-frequency plateau reveals the capacitance of a cation depletion layer. This knowledge can be used to calculate the ionic density.

Until now, we have neglected TLs, simplifying the field drop. Implementing TLs experimentally will significantly alter the energy levels in the device by, for example, redistributing the built-in voltage from the workfunction-difference of the contact layers<sup>52</sup> or changing surface dipoles.<sup>53</sup> However, omitting TLs in the experiment might alter the perovskite crystallization or induce oxidation reactions between the electrodes and the perovskite, which might have an impact on the ion density.

Therefore, it is beneficial to perform measurements on the whole device stack.

Introducing TLs into the simulation reduces the low-frequency capacitance, which results in a downturn in the calculated ionic densities in Figure 5a (purple line). The reason for this is the significant fraction of the built-in-voltage that now drops across the TLs, which depends on the input ion density. At high ionic densities, almost no field drop across the perovskite is observed (Supplementary Figure S14). On the other hand, this introduces additional capacitive layers, that distort the capacitive behavior. In this case, the magnitude of the TL-induced alteration depends on various parameters such as its dielectric constant and its thickness (Supplementary Figure S15). However, this can be accounted for by differentiating eq 5 with respect to  $V_{\text{app}}$ , which yields the Mott–Schottky equation

$$\frac{d(C_{\text{depl}}^{-2})}{dV_{\text{app}}} = -\frac{2}{n_{\text{ion}} e \epsilon \epsilon_0} \quad (6)$$

Therefore, the only inputs we need in order to calculate the ionic density are the perovskite dielectric constant and the low-frequency capacitance at various voltages, as the TL-induced distortion of the internal voltage has no influence on the slope. However, since the layer-distributed voltage still impacts the intercept, unfortunately this technique cannot be used to obtain the  $V_{\text{bi}}$  by extending the slope to the  $x$ -axis. It is important to note that a frequency within the low-frequency plateau of the C-f spectrum (<5 Hz in our case) should be chosen<sup>54</sup> in order to ensure that the ionic capacitance is dominant as both the high- and intermediate-frequency capacitances are not directly linked to ionic density (rather to electronic charges), as discussed in Supplementary Note S2. That is why the Mott–Schottky analysis at intermediate frequencies ( $f = 10^4\text{--}10^5 \text{ Hz}$ ) yields different results from the one at low frequencies, as shown in Supplementary Figure S16. Furthermore, long enough equilibration times at each voltage point should be used in order to avoid transient behavior that may interfere with the capacitive response.<sup>54</sup> In our case, using a slow sweep speed of  $3 \times 10^{-3} \text{ V/s}$  revealed little to no hysteretic behavior, as Supplementary Figure S17 reveals.

Figure 5b shows the linear dependence between  $C^{-2}$  and the applied voltage in the simulation and the experiment. As expected from eq 6, the slope decreases for higher ionic densities. To validate this method experimentally, we perform

low-frequency Mott–Schottky measurements before and after aging a triple cation cell under 1-sun conditions. Since low-frequency capacitance measurement may be inherently noisy, it is important to average sufficiently long and to measure over a sufficiently large voltage range to identify the linear region and get the best slope fit. In our case we used voltages from  $-0.2$  to  $0.3$  V. Initially, we obtain a mobile ion density of  $2.4 \times 10^{17}$  cm $^{-3}$  which lies within the range of reported values. As expected, the slope declines for longer aging times (Figure 5c) due to the light-induced increase of the mobile ion density.<sup>55</sup> In our case, the mobile ion density triples after 5 h of light-soaking which explains the increase of ionic losses over time.<sup>56</sup> We note that we assumed here that the dielectric constant in eq 6 refers to the perovskite. However, an effective dielectric constant may be considered for multilayer devices, especially for devices with thicker TLs. Nevertheless, Figure 5a shows that this does not cause significant deviations of the prediction to the input for our devices with thin TLs. This figure further highlights that low-frequency Mott–Schottky analysis (yellow line) can be used to accurately obtain mobile ion densities for ionic densities higher than the electrode charge, which complements the low ion density determination capabilities of BACE very well.

Using the drift-diffusion simulation tool SETFOS, we examined the impact of mobile ions based on various transient experimental methodologies, including JV scans with different scan rates. We can reproduce hysteresis effects and the dependence of PCE on the scan speed. We find that ionic accumulation at the interfaces screens the field and hinders charge extraction, which explains the aforementioned dependence. We then evaluated CELIV, BACE, and C-f-measurements on their ability to determine mobile ion densities accurately. CELIV measurements are rather poorly suited to do this because of initial distribution of ions under short-circuit conditions as well as the required long extraction times which lead to an underestimation of ions. Integrating currents obtained by BACE measurements over the ion-dominated regime, on the other hand, yields the correct ion density as long as it is lower than the CV/ed-charge. Above this value, further ion migration is hindered by field screening. The potential distribution across the perovskite reveals that most of the field drops across the cation depletion layer.

Therefore, the low-frequency capacitance is related to the depletion layer rather than the accumulation layer, although the mobile ion density cannot be deduced from the capacitance step in the case of 2 oppositely charged mobile ion species. Nevertheless, in case of 1 dominant mobile excess species (such as halide vacancies), using the depletion layer equation, ion densities above the CV-charge can be accurately determined for perovskite devices without transport layers. For complete device stacks, we propose and perform Mott–Schottky analysis at low frequencies to obtain high ion densities in device stack measurements above the CV/ed charge density. For a standard triple cation-based *pin*-type device, we obtain a mobile ion density of  $2.4 \times 10^{17}$  cm $^{-3}$ , which rises to  $7.5 \times 10^{17}$  cm $^{-3}$  after 5 h under 1 sun equivalent illumination and open-circuit conditions. Although the analysis of low-frequency capacitance measurements must be approached with experimental caution, we find that this technique complements well with BACE for the detection of low ion density below the CV/ed charge density, which allows for reliable determination of mobile ion density across a large range of values. The insights obtained in this work provide the

opportunity to further investigate the mechanisms behind mobile-ion induced efficiency and degradation losses in different perovskite compositions or the impact of different material deposition techniques toward mitigating their detrimental impact in the future.

## ■ ASSOCIATED CONTENT

### Data Availability Statement

The data that support the findings of this study are available from the corresponding author upon reasonable request.

### SI Supporting Information

The Supporting Information is available free of charge at <https://pubs.acs.org/doi/10.1021/acs.jpcllett.3c00530>.

Experimental methods of device fabrication and characterization techniques, drift-diffusion model description (Supplementary Note S1); frequency-dependent capacitance model (Supplementary Note S2); simulation parameters (Supplementary Table S1); influence of charge carrier mobility on C-f spectra (Supplementary Figure S1); steady-state charge carrier densities (Supplementary Figure S2); back-to-back fast hysteresis PCE measurements (Supplementary Figure S3); hysteresis spectra of  $V_{OC}$ , FF, and  $J_{SC}$  (Supplementary Figure S4); cation density distribution at various voltages and scan speeds (Supplementary Figure S5); electron and hole distribution at short-circuit conditions (Supplementary Figure S6); CELIV and BACE transients for varying ion mobilities (Supplementary Figure S7); CELIV transients for long ramp times (Supplementary Figure S8); CELIV and BACE transients for varying mobile anion densities (Supplementary Figure S9); CELIV transients with preconditioning at  $V_{bi}$  (Supplementary Figure S10); Nyquist plots for the standard parameter simulation (Supplementary Figure S11); C-f curve for various series resistances (Supplementary Figure S12); C-f curve with constant mobile cation density and various mobile anion densities (Supplementary Figure S13); potential drop across the device for various ion densities (Supplementary Figure S14); calculated ion densities from depletion layer equation for different TL configurations (Supplementary Figure S15); MS plots for different ion densities at intermediate and low frequencies (Supplementary Figure S16); low-frequency Mott–Schottky hysteresis measurements (Supplementary Figure S17); reverse bias JV measurement and CELIV transients for various averaging counts (Supplementary Figure S18); JV measurement for various averaging counts (Supplementary Figure S19) ([PDF](#))

## ■ AUTHOR INFORMATION

### Corresponding Author

Martin Stolterfoht – Institute of Physics and Astronomy,  
University of Potsdam, D-14476 Potsdam-Golm, Germany;  
 [orcid.org/0000-0002-4023-2178](https://orcid.org/0000-0002-4023-2178); Email: [stolterf@unipotsdam.de](mailto:stolterf@unipotsdam.de)

### Authors

Jonas Diekmann – Institute of Physics and Astronomy,  
University of Potsdam, D-14476 Potsdam-Golm, Germany

Francisco Peña-Camargo – Institute of Physics and Astronomy, University of Potsdam, D-14476 Potsdam-Golm, Germany; [ORCID iD](https://orcid.org/0000-0002-8402-4266)

Nurlan Tokmoldin – Institute of Physics and Astronomy, University of Potsdam, D-14476 Potsdam-Golm, Germany; [ORCID iD](https://orcid.org/0000-0002-0663-0228)

Jarla Thiesbrummel – Institute of Physics and Astronomy, University of Potsdam, D-14476 Potsdam-Golm, Germany

Jonathan Warby – Institute of Physics and Astronomy, University of Potsdam, D-14476 Potsdam-Golm, Germany; [ORCID iD](https://orcid.org/0000-0003-3518-173X)

Emilio Gutierrez-Partida – Institute of Physics and Astronomy, University of Potsdam, D-14476 Potsdam-Golm, Germany

Sahil Shah – Institute of Physics and Astronomy, University of Potsdam, D-14476 Potsdam-Golm, Germany

Dieter Neher – Institute of Physics and Astronomy, University of Potsdam, D-14476 Potsdam-Golm, Germany; [ORCID iD](https://orcid.org/0000-0001-6618-8403)

Complete contact information is available at:  
<https://pubs.acs.org/10.1021/acs.jpcllett.3c00530>

## Notes

The authors declare no competing financial interest.

## ACKNOWLEDGMENTS

We acknowledge HyPerCells (a joint graduate school of the University of Potsdam and the Helmholtz-Zentrum Berlin) and the Deutsche Forschungsgemeinschaft (DFG, German Research Foundation) - project number 423749265 and 424709669 - SPP 2196 (SURPRISE-2 and HIPSTER-PRO) for funding. We also acknowledge financial support by the Federal Ministry for Economic Affairs and Energy within the framework of the seventh Energy Research Programme (P3T-HOPE, 03EE1017C). M.S. further acknowledges the Heisenberg program from the Deutsche Forschungsgemeinschaft (DFG, German Research Foundation) for funding, project number 498155101.

## REFERENCES

- (1) Yoo, J. J.; Seo, G.; Chua, M. R.; Park, T. G.; Lu, Y.; Rotermund, F.; Kim, Y. K.; Moon, C. S.; Jeon, N. J.; Correa-Baena, J. P.; Bulović, V.; Shin, S. S.; Bawendi, M. G.; Seo, J. Efficient Perovskite Solar Cells via Improved Carrier Management. *Nature* **2021**, *590* (7847), 587–593.
- (2) Yoshikawa, K.; Kawasaki, H.; Yoshida, W.; Irie, T.; Konishi, K.; Nakano, K.; Uto, T.; Adachi, D.; Kanematsu, M.; Uzu, H.; Yamamoto, K. Silicon Heterojunction Solar Cell with Interdigitated Back Contacts for a Photoconversion Efficiency over 26%. *Nat. Energy* **2017**, *2* (5), 17032.
- (3) Courtier, N. E.; Cave, J. M.; Foster, J. M.; Walker, A. B.; Richardson, G. How Transport Layer Properties Affect Perovskite Solar Cell Performance: Insights from a Coupled Charge Transport/Ion Migration Model. *Energy Environ. Sci.* **2019**, *12* (1), 396–409.
- (4) Hoke, E. T.; Slotcavage, D. J.; Dohner, E. R.; Bowring, A. R.; Karunadasa, H. I.; McGehee, M. D. Reversible Photo-Induced Trap Formation in Mixed-Halide Hybrid Perovskites for Photovoltaics. *Chem. Sci.* **2015**, *6* (1), 613–617.
- (5) Thiesbrummel, J.; Le Corre, V. M.; Peña-Camargo, F.; Perdigón-Toro, L.; Lang, F.; Yang, F.; Grischek, M.; Gutierrez-Partida, E.; Warby, J.; Farrar, M. D.; Mahesh, S.; Caprioglio, P.; Albrecht, S.; Neher, D.; Snaith, H. J.; Stolterfoht, M. Universal Current Losses in Perovskite Solar Cells Due to Mobile Ions. *Adv. Energy Mater.* **2021**, *11*, 2101447.
- (6) Wu, N.; Wu, Y.; Walter, D.; Shen, H.; Duong, T.; Grant, D.; Barugkin, C.; Fu, X.; Peng, J.; White, T.; Catchpole, K.; Weber, K. Identifying the Cause of Voltage and Fill Factor Losses in Perovskite Solar Cells by Using Luminescence Measurements. *Energy Tech.* **2017**, 1827–1835.
- (7) Khenkin, M. V.; Katz, E. A.; Abate, A.; Bardizza, G.; Berry, J. J.; Brabec, C.; Brunetti, F.; Bulović, V.; Burlingame, Q.; Di Carlo, A.; Cheacharoen, R.; Cheng, Y.-B.; Colsmann, A.; Cros, S.; Domanski, K.; Dusza, M.; Fell, C. J.; Forrest, S. R.; Galagan, Y.; Di Girolamo, D.; Grätzel, M.; Hagfeldt, A.; von Hauff, E.; Hoppe, H.; Kettle, J.; Köbler, H.; Leite, M. S.; Liu, S.; Loo, Y.-L.; Luther, J. M.; Ma, C.-Q.; Madsen, M.; Manceau, M.; Matheron, M.; McGehee, M.; Meitzner, R.; Nazeeruddin, M. K.; Nogueira, A. F.; Odabaşı, Ç.; Osheroval, A.; Park, N.-G.; Reese, M. O.; De Rossi, F.; Saliba, M.; Schubert, U. S.; Snaith, H. J.; Stranks, S. D.; Tress, W.; Troshin, P. A.; Turkovic, V.; Veenstra, S.; Visoly-Fisher, I.; Walsh, A.; Watson, T.; Xie, H.; Yıldırım, R.; Zakeeruddin, S. M.; Zhu, K.; Lira-Cantu, M. Consensus Statement for Stability Assessment and Reporting for Perovskite Photovoltaics Based on ISOS Procedures. *Nat. Energy* **2020**, *5* (1), 35–49.
- (8) Fu, F.; Pisoni, S.; Jeangros, Q.; Sastre-Pellicer, J.; Kawecki, M.; Paracchino, A.; Moser, T.; Werner, J.; Andres, C.; Duchêne, L.; Fiala, P.; Rawlence, M.; Nicolay, S.; Ballif, C.; Tiwari, A. N.; Buecheler, S. I2 Vapor-Induced Degradation of Formamidinium Lead Iodide Based Perovskite Solar Cells under Heat–Light Soaking Conditions. *Energy Environ. Sci.* **2019**, *12* (10), 3074–3088.
- (9) Kundu, S.; Kelly, T. L. In Situ Studies of the Degradation Mechanisms of Perovskite Solar Cells. *EcoMat* **2020**, *2* (2), 1–22.
- (10) Bryant, D.; Aristidou, N.; Pont, S.; Sanchez-Molina, I.; Chotchunangatchaval, T.; Wheeler, S.; Durrant, J. R.; Haque, S. A. Light and Oxygen Induced Degradation Limits the Operational Stability of Methylammonium Lead Triiodide Perovskite Solar Cells. *Energy Environ. Sci.* **2016**, *9* (5), 1655–1660.
- (11) Peters, I. M.; Rodriguez Gallegos, C. D.; Sofia, S. E.; Buonassisi, T. The Value of Efficiency in Photovoltaics. *Joule* **2019**, *3* (11), 2732–2747.
- (12) Dunfield, S. P.; Bliss, L.; Zhang, F.; Luther, J. M.; Zhu, K.; van Hest, M. F. A. M.; Reese, M. O.; Berry, J. J. From Defects to Degradation: A Mechanistic Understanding of Degradation in Perovskite Solar Cell Devices and Modules. *Adv. Energy Mater.* **2020**, *10* (26), 1904054.
- (13) Braly, I. L.; Hillhouse, H. W. Optoelectronic Quality and Stability of Hybrid Perovskites from MAPbI<sub>3</sub> to MAPbI<sub>2</sub>Br Using Composition Spread Libraries. *J. Phys. Chem. C* **2016**, *120* (2), 893–902.
- (14) Divitini, G.; Cacovich, S.; Matteocci, F.; Cinà, L.; Di Carlo, A.; Ducati, C. In Situ Observation of Heat-Induced Degradation of Perovskite Solar Cells. *Nat. Energy* **2016**, *1* (1), 15012 DOI: [10.1038/nenergy.2015.12](https://doi.org/10.1038/nenergy.2015.12).
- (15) Zhao, J.; Deng, Y.; Wei, H.; Zheng, X.; Yu, Z.; Shao, Y.; Shield, J. E.; Huang, J. Strained Hybrid Perovskite Thin Films and Their Impact on the Intrinsic Stability of Perovskite Solar Cells. *Sci. Adv.* **2017**, *3* (11), eaao5616 DOI: [10.1126/sciadv.aao5616](https://doi.org/10.1126/sciadv.aao5616).
- (16) Van Reenen, S.; Kemerink, M.; Snaith, H. J. Modeling Anomalous Hysteresis in Perovskite Solar Cells. *J. Phys. Chem. Lett.* **2015**, *6* (19), 3808–3814.
- (17) Abdi-Jalebi, M.; Andaji-Garmaroudi, Z.; Cacovich, S.; Stavrakas, C.; Philippe, B.; Richter, J. M.; Alsari, M.; Booker, E. P.; Hutter, E. M.; Pearson, A. J.; Lilliu, S.; Savenije, T. J.; Rensmo, H.; Divitini, G.; Ducati, C.; Friend, R. H.; Stranks, S. D. Maximizing and Stabilizing Luminescence from Halide Perovskites with Potassium Passivation. *Nature* **2018**, *555* (7697), 497–501.
- (18) Eames, C.; Frost, J. M.; Barnes, P. R. F.; O'Regan, B. C.; Walsh, A.; Islam, M. S. Ionic Transport in Hybrid Lead Iodide Perovskite Solar Cells. *Nat. Commun.* **2015**, *6* (May), 2–9.
- (19) Kumawat, N. K.; Tress, W.; Gao, F. Mobile Ions Determine the Luminescence Yield of Perovskite Light-Emitting Diodes under Pulsed Operation. *Nat. Commun.* **2021**, *12* (1), 1–8.
- (20) Bertoluzzi, L.; Boyd, C. C.; Rolston, N.; Xu, J.; Prasanna, R.; O'Regan, B. C.; McGehee, M. D. Mobile Ion Concentration

- Measurement and Open Access Band Diagram Simulation Platform for Halide Perovskite Solar Cells. *Joule* **2020**, *4*, 109.
- (21) Cheng, Y.; Li, H. W.; Qing, J.; Yang, Q. D.; Guan, Z.; Liu, C.; Cheung, S. H.; So, S. K.; Lee, C. S.; Tsang, S. W. The Detrimental Effect of Excess Mobile Ions in Planar  $\text{CH}_3\text{NH}_3\text{PbI}_3$  Perovskite Solar Cells. *J. Mater. Chem. A* **2016**, *4* (33), 12748–12755.
- (22) Almora, O.; Zarazua, I.; Mas-Marza, E.; Mora-Sero, I.; Bisquert, J.; Garcia-Belmonte, G. Capacitive Dark Currents, Hysteresis, and Electrode Polarization in Lead Halide Perovskite Solar Cells. *J. Phys. Chem. Lett.* **2015**, *6* (9), 1645–1652.
- (23) Reichert, S.; An, Q.; Woo, Y. W.; Walsh, A.; Vaynzof, Y.; Deibel, C. Probing the Ionic Defect Landscape in Halide Perovskite Solar Cells. *Nat. Commun.* **2020**, *11* (1), 6098 DOI: [10.1038/s41467-020-19769-8](https://doi.org/10.1038/s41467-020-19769-8).
- (24) Futscher, M. H.; Lee, J. M.; McGovern, L.; Muscarella, L. A.; Wang, T.; Haider, M. I.; Fakharuddin, A.; Schmidt-Mende, L.; Ehrler, B. Quantification of Ion Migration in  $\text{CH}_3\text{NH}_3\text{PbI}_3$  Perovskite Solar Cells by Transient Capacitance Measurements. *Mater. Horizons* **2019**, *6* (7), 1497–1503.
- (25) Birkhold, S. T.; Precht, J. T.; Giridharagopal, R.; Eperon, G. E.; Schmidt-Mende, L.; Ginger, D. S. Direct Observation and Quantitative Analysis of Mobile Frenkel Defects in Metal Halide Perovskites Using Scanning Kelvin Probe Microscopy. *J. Phys. Chem. C* **2018**, *122* (24), 12633–12639.
- (26) Weber, S. A. L.; Hermes, I. M.; Turren-Cruz, S. H.; Gort, C.; Bergmann, V. W.; Gilson, L.; Hagfeldt, A.; Graetzel, M.; Tress, W.; Berger, R. How the Formation of Interfacial Charge Causes Hysteresis in Perovskite Solar Cells. *Energy Environ. Sci.* **2018**, *11* (9), 2404–2413.
- (27) Walsh, A.; Scanlon, D. O.; Chen, S.; Gong, X. G.; Wei, S. H. Self-Regulation Mechanism for Charged Point Defects in Hybrid Halide Perovskites. *Angew. Chemie Int. Ed.* **2015**, *54* (6), 1791–1794.
- (28) Bertoluzzi, L.; Belisle, R. A.; Bush, K. A.; Cheacharoen, R.; McGehee, M. D.; O'Regan, B. C. In Situ Measurement of Electric-Field Screening in Hysteresis-Free PTAAs/FA0.83Cs0.17Pb-(0.83Br0.17)3/C60 Perovskite Solar Cells Gives an Ion Mobility of  $\sim 3 \times 10^{-7}$   $\text{cm}^2/(\text{V s})$ , 2 Orders of Magnitude Faster than Reported for Metal-Oxide-Contacted Perovskite. *C. J. Am. Chem. Soc.* **2018**, *140* (40), 12775–12784.
- (29) Euvrard, J.; Gunawan, O.; Mitzi, D. B. Impact of PbI<sub>2</sub> Passivation and Grain Size Engineering in  $\text{CH}_3\text{NH}_3\text{PbI}_3$  Solar Absorbers as Revealed by Carrier-Resolved Photo-Hall Technique. *Adv. Energy Mater.* **2019**, *9* (47), 1902706.
- (30) Peña-Camargo, F.; Thiesbrummel, J.; Hempel, H.; Musienko, A.; Le Corre, V. M.; Diekmann, J.; Warby, J.; Unold, T.; Lang, F.; Neher, D.; Stolterfoht, M. Revealing the Doping Density in Perovskite Solar Cells and Its Impact on Device Performance. *Appl. Phys. Rev.* **2022**, *9* (2), 021409.
- (31) Fischer, M.; Tvingstedt, K.; Baumann, A.; Dyakonov, V. Doping Profile in Planar Hybrid Perovskite Solar Cells Identifying Mobile Ions. *ACS Appl. Energy Mater.* **2018**, *1* (10), 5129–5134.
- (32) Stolterfoht, M.; Wolff, C. M.; Márquez, J. A.; Zhang, S.; Hages, C. J.; Rothhardt, D.; Albrecht, S.; Burn, P. L.; Meredith, P.; Unold, T.; Neher, D. Visualization and Suppression of Interfacial Recombination for High-Efficiency Large-Area Pin Perovskite Solar Cells. *Nat. Energy* **2018**, *3* (10), 847.
- (33) Diekmann, J.; Caprioglio, P.; Futscher, M. H.; Le Corre, V. M.; Reichert, S.; Jaiser, F.; Arvind, M.; Toro, L. P.; Gutierrez-Partida, E.; Peña-Camargo, F.; Deibel, C.; Ehrler, B.; Unold, T.; Kirchartz, T.; Neher, D.; Stolterfoht, M. Pathways toward 30% Efficient Single-Junction Perovskite Solar Cells and the Role of Mobile Ions. *Sol. RRL* **2021**, *5* (8), 2100219.
- (34) Le Corre, V. M.; Diekmann, J.; Peña-Camargo, F.; Thiesbrummel, J.; Tokmoldin, N.; Gutierrez-Partida, E.; Peters, K. P.; Perdigón-Toro, L.; Futscher, M. H.; Lang, F.; Warby, J.; Snaith, H. J.; Neher, D.; Stolterfoht, M. Quantification of Efficiency Losses Due to Mobile Ions in Perovskite Solar Cells via Fast Hysteresis Measurements. *Sol. RRL* **2022**, *6* (4), 2100772.
- (35) Futscher, M. H.; Gangishetty, M. K.; Congreve, D. N.; Ehrler, B. Quantifying Mobile Ions and Electronic Defects in Perovskite-Based Devices with Temperature-Dependent Capacitance Measurements: Frequency vs Time Domain. *J. Chem. Phys.* **2020**, *152* (4), 044202.
- (36) Senocrate, A.; Moudrakovski, I.; Kim, G. Y.; Yang, T. Y.; Gregori, G.; Grätzel, M.; Maier, J. The Nature of Ion Conduction in Methylammonium Lead Iodide: A Multimethod Approach. *Angew. Chemie - Int. Ed.* **2017**, *56* (27), 7755–7759.
- (37) Li, C.; Guerrero, A.; Huettner, S.; Bisquert, J. Unravelling the Role of Vacancies in Lead Halide Perovskite through Electrical Switching of Photoluminescence. *Nat. Commun.* **2018**, *9* (1), 1–8.
- (38) García-Batlle, M.; Deumel, S.; Huerdler, J. E.; Tedde, S. F.; Almora, O.; García-Belmonte, G. Effective Ion Mobility and Long-Term Dark Current of Metal Halide Perovskites with Different Crystallinities and Compositions. *Adv. Photonics Res.* **2022**, *3* (12), 2200136.
- (39) Jacobs, D. A.; Wu, Y.; Shen, H.; Barugkin, C.; Beck, F. J.; White, T. P.; Weber, K.; Catchpole, K. R. Hysteresis Phenomena in Perovskite Solar Cells: The Many and Varied Effects of Ionic Accumulation. *Phys. Chem. Chem. Phys.* **2017**, *19* (4), 3094–3103.
- (40) Wu, F.; Bahrami, B.; Chen, K.; Mabrouk, S.; Pathak, R.; Tong, Y.; Li, X.; Zhang, T.; Jian, R.; Qiao, Q. Bias-Dependent Normal and Inverted J- v Hysteresis in Perovskite Solar Cells. *ACS Appl. Mater. Interfaces* **2018**, *10* (30), 25604–25613.
- (41) Sandberg, O. J.; Nyman, M.; Österbacka, R. Direct Determination of Doping Concentration and Built-in Voltage from Extraction Current Transients. *Org. Electron.* **2014**, *15* (11), 3413–3420.
- (42) Juška, G.; Arlauskas, K.; Viliūnas, M.; Kočka, J. Extraction Current Transients: New Method of Study of Charge Transport in Microcrystalline Silicon. *Phys. Rev. Lett.* **2000**, *84* (21), 4946–4949.
- (43) Belisle, R. A.; Nguyen, W. H.; Bowring, A. R.; Calado, P.; Li, X.; Irvine, S. J. C.; McGehee, M. D.; Barnes, P. R. F.; O'Regan, B. C. Interpretation of Inverted Photocurrent Transients in Organic Lead Halide Perovskite Solar Cells: Proof of the Field Screening by Mobile Ions and Determination of the Space Charge Layer Widths. *Energy Environ. Sci.* **2017**, *10* (1), 192–204.
- (44) Kniepert, J.; Paulke, A.; Perdigón-Toro, L.; Kurpiers, J.; Zhang, H.; Gao, F.; Yuan, J.; Zou, Y.; Le Corre, V. M.; Koster, L. J. A.; Neher, D. Reliability of Charge Carrier Recombination Data Determined with Charge Extraction Methods. *J. Appl. Phys.* **2019**, *126* (20), 205501.
- (45) Fischer, M.; Kiermasch, D.; Gil-Escríg, L.; Bolink, H. J.; Dyakonov, V.; Tvingstedt, K. Assigning Ionic Properties in Perovskite Solar Cells: a Unifying Transient Simulation/Experimental Study. *Sustain. Energy Fuels* **2021**, *5* (14), 3578–3587.
- (46) Yang, J. H.; Yin, W. J.; Park, J. S.; Wei, S. H. Fast Self-Diffusion of Ions in  $\text{CH}_3\text{NH}_3\text{PbI}_3$ : The Interstitially Mechanism versus Vacancy-Assisted Mechanism. *J. Mater. Chem. A* **2016**, *4* (34), 13105–13112.
- (47) Mizusaki, J.; Arai, K.; Fueki, K. Ionic Conduction of the Perovskite-Type Halides. *Solid State Ionics* **1983**, *11* (3), 203–211.
- (48) Yoon, S. J.; Kuno, M.; Kamat, P. V. Shift Happens: How Halide Ion Defects Influence Photoinduced Segregation in Mixed Halide Perovskites. *ACS Energy Lett.* **2017**, *2* (7), 1507–1514.
- (49) Ravishankar, S.; Liu, Z.; Rau, U.; Kirchartz, T. Multilayer Capacitances: How Selective Contacts Affect Capacitance Measurements of Perovskite Solar Cells. *PRX Energy* **2022**, *1* (1), 013003.
- (50) Ravishankar, S.; Unold, T.; Kirchartz, T. Comment on “Resolving Spatial and Energetic Distributions of Trap States in Metal Halide Perovskite Solar Cells. *Science (80.)* **2021**, *371* (6532), eabd8014 DOI: [10.1126/science.abd8014](https://doi.org/10.1126/science.abd8014).
- (51) Siekmann, J.; Ravishankar, S.; Kirchartz, T. Apparent Defect Densities in Halide Perovskite Thin Films and Single Crystals. *ACS Energy Letters* **2021**, *6*, 3244–3251.
- (52) Kato, Y.; Ono, L. K.; Lee, M. V.; Wang, S.; Raga, S. R.; Qi, Y. Silver Iodide Formation in Methyl Ammonium Lead Iodide

Perovskite Solar Cells with Silver Top Electrodes. *Adv. Mater. Interfaces* **2015**, 2 (13), 1500195.

(53) Chen, L.; Chen, Q.; Wang, C.; Li, Y. Interfacial Dipole in Organic and Perovskite Solar Cells. *J. Am. Chem. Soc.* **2020**, 142 (43), 18281–18292.

(54) Almora, O.; Aranda, C.; Mas-Marzá, E.; Garcia-Belmonte, G. On Mott-Schottky Analysis Interpretation of Capacitance Measurements in Organometal Perovskite Solar Cells. *Appl. Phys. Lett.* **2016**, 109 (17), 173903.

(55) Joshi, P. H.; Zhang, L.; Hossain, I. M.; Abbas, H. A.; Kottokaran, R.; Nehra, S. P.; Dhaka, M.; Noack, M.; Dalal, V. L. The Physics of Photon Induced Degradation of Perovskite Solar Cells. *AIP Adv.* **2016**, 6 (11), 115114.

(56) Hong, J.; Kim, H.; Hwang, I. Aging-Induced Light-Soaking Effects and Open-Circuit Voltage Hysteretic Behavior of Inverted Perovskite Solar Cells Incorporating a Hole Transport Metal Halide Layer via Morphology-Dependent Inflow of Iodide Ions. *J. Mater. Chem. C* **2019**, 7 (5), 1173–1181.

**Supplementary Information**

**Determination of Mobile Ion Densities in Halide Perovskites via Low-Frequency Capacitance and Charge Extraction Techniques**

Jonas Diekmann<sup>1</sup>, Francisco Peña-Camargo<sup>1</sup>, Nurlan Tokmoldin<sup>1</sup>, Jarla Thiesbrummel<sup>1</sup>, Jonathan Warby<sup>1</sup>, Emilio Gutierrez-Partida<sup>1</sup>, Sahil Shah<sup>1</sup>, Dieter Neher<sup>1</sup>, Martin Stolterfoht<sup>1\*</sup>

\*email: [stolterf@unipotsdam.de](mailto:stolterf@unipotsdam.de)

<sup>1</sup>Institute of Physics and Astronomy, University of Potsdam, D-14476 Potsdam-Golm, Germany

## Experimental Methods

**Device Fabrication of pin-type cells:** *Substrates and HTL:* Pre-patterned 2.5x2.5 cm<sup>2</sup> 15 Ω/sq. ITO substrates (Automatic Research, Germany) were cleaned with acetone, 3% Hellmanex solution, DI-water and iso-propanol, by sonication for 10 min in each solution. After a microwave plasma treatment (3 min, 200 W), the samples were transferred to a N<sub>2</sub>-filled glovebox. A PTAA (Sigma-Aldrich) layer with a thickness of 8 nm was spin-coated from a 1.5 mg mL<sup>-1</sup> PTAA/toluene solution at 6000 rpm for 30 seconds. After 10 min annealing on a hotplate at 100 °C, the films were cooled down to room temperature and a 60 μL solution of PFN-Br (1-Material, 0.5 mg/mL in methanol) was deposited onto PTAA while the substrate was being spun at 5000 rpm for 20 s resulting in a film with thickness below the detection limit of our AFM (< 5 nm). No further annealing occurred.

**Perovskite solutions:** The triple cation perovskite solutions were prepared by mixing two 1.2 M FAPbI<sub>3</sub> and MAPbBr<sub>3</sub> perovskite solutions in DMF:DMSO (4:1 volume ratio, v:v) in a ratio of 83:17 (for the 83:17 triple cation reference cell). The 1.2 M FAPbI<sub>3</sub> solution was thereby prepared by dissolving FAI (722 mg) and PbI<sub>2</sub> (2130 mg) in 2.8 mL DMF and 0.7 mL DMSO which contains a 10 molar% excess of PbI<sub>2</sub>. The 1.2 M MAPbBr<sub>3</sub> solution was made by dissolving MABr (470 mg) and PbBr<sub>2</sub> (1696 mg) in 2.8 mL DMF and 0.7 mL DMSO which contains a 10 molar% excess of PbBr<sub>2</sub>. Lastly, 40 μL of a 1.5 CsI solution in DMSO (389 mg CsI in 1 mL DMSO) was mixed with 960 μL of the MAFA solution resulting in a nominal perovskite stoichiometry of Cs<sub>0.05</sub>(FA<sub>0.83</sub>MA<sub>0.17</sub>)<sub>0.95</sub>Pb(I<sub>0.83</sub>Br<sub>0.17</sub>)<sub>3</sub>.

**Perovskite film fabrication:** The film was deposited by spin-coating at 5000 rpm for 35 s and 10 s after the start of the spinning process, the spinning substrate was washed with 300 μL ethylacetate for approximately 1 s (the anti-solvent was placed in the center of the film). We note, that by the end of the spinning process the perovskite film turned dark brown. The perovskite film was then annealed at 100 °C for 1 h on a preheated hotplate where the film turned slightly darker.

**ETL and Top Contact:** After annealing, the samples were transferred to an evaporation chamber where fullerene-C<sub>60</sub> (30 nm), 2,9-Dimethyl-4,7-diphenyl-1,10-phenanthroline BCP (8 nm) and copper (100 nm) were deposited under vacuum ( $p = 10^{-7}$  mbar). The overlap of the copper and the ITO electrodes defined the active area of the pixel (6 mm<sup>2</sup>).

**Fast-hysteresis measurements:** Fast JV-curves were obtained by applying a triangular voltage pulse to the cells starting from approximately open-circuit ( $V_{OC}$ ) followed by a reverse sweep from open-circuit to -0.1 V and forward sweep from -0.1 V to  $V_{OC}$  with variable frequency or scan speed (V/s). The duration of the hold voltage at  $V_{OC}$  was 5x longer than the total scan time of the voltage sweep. The scan speed time was thereby varied and the voltage response of the cell measured with an Siglent SDS1202X USB Oscilloscope, using an external load resistance of 10 Ohm. The voltage pulse was supplied by an SDG1000X Siglent function generator in combination with a home-built power amplifier (4x).

**Charge extraction by linearly increasing voltage (dark-CELIV):** In dark dark-CELIV the device was initially held at short-circuit conditions. Then the voltage was linearly increased to minus 0.4 V (in reverse bias) using a pulse generator. The slope ( $S$ ) was thereby varied to assess a wide timescale range. The current transients were recorded with an oscilloscope (Agilent DSO9104H) and measured with a variable load resistance (50 Ω at short 10 μs pulse and up to 10 kΩ at 100 ms pulses) to keep the voltage response approximately constant. The increased load resistance reduces the time resolution at short times but allows to record the response for long pulses. Therefore, with decreasing slope, the load resistance is increased to compensate the reduced current (which is proportional to the slope). The continuous increase of the electrode charge leads to a step-like voltage response. The

voltage response step of the cell is given by  $\Delta V = AR_{load}C$  from which we calculated the capacitance of the cell ( $C$ ). Then, for each transient the capacitance is plotted and the envelop can be considered as the overall capacitance transient.<sup>1</sup> Equilibrium charges in the active layer (doping-induced electronic charge or mobile ions) lead to an additional bump in the voltage response.

**Bias-assisted charge extraction (BACE):** In dark BACE, the device was initially held at a voltage close to the open-circuit voltage ( $V_{pre}$ ) where the injected charge equals the short-circuit current. After a pre-set delay time, a bias  $V_{coll} = 0V$  (or a reverse bias), was applied to extract the injected and capacitive charge in the device. The delay times was chosen to be typically 5x longer than the extraction time of charges observed under the collection bias (typically 50 s to 1000 s) in order to allow ionic charges to distribute throughout the active layer. The current transients were measured with a Keithley 2400 using a home-built LabView program. The use of a current-meter was found to be necessary over an oscilloscope to resolve the small ion drift currents and we note that no significant differences were observed when the measurements were performed with a Keithley 485 Picoamperemeter instead of the Keithley 2400. Finally, the extracted charge was obtained by integrating the current transient and the charge carrier density by dividing the total charge by the elementary charge and the cell volume.

**Light aging:** Light aging under open-circuit conditions was performed in a dedicated aging box in the glovebox under N<sub>2</sub> atmosphere under using white LED array illumination providing a 1 sun equivalent intensity by matching the initial current of the cell to the  $J_{sc}$ . The intensity of the LED was checked using a photodiode and remained stable over the course of the measurement timescale (~24 h) in a sample holder. The cells were cooled to 25 °C over the course of the measurement using a Peltier element, however, no significant changes in the degradation was observed without additional cooling.

**Capacitance measurement:** Frequency and voltage dependent capacitance measurements were performed using 2 different setups. The first setup is based on the commercial Impedance Network Analyzer Keysight E5061B. The measurements were performed in reflection mode with Port 1 using an impedance of 50 Ohm. However, a significant noise in the measured capacitance was observed at low frequencies (e.g. 1 Hz). To improve the resolution, a custom-built setup was used consisting of a Siglent SDS1202X USB Oscilloscope with a variable external load resistance (10 Ohm – 1 MOhm). The voltage pulse consisting of a small perturbation sine wave with amplitude of 50 mV was supplied by an SDG1000X Siglent function generator. For voltage dependent measurements, the applied sine wave was superimposed by a constant DC voltage applied to the cell (analogously to measuring a JV curve). The response of the cell which represents a phase sifted sine wave was also recorded with the same Oscilloscope. The phase angle ( $\delta$ ) between the applied and the response voltage was calculated by fitting both waves with a sinus waveform. A Python routine was used to automate the measurement procedure and to calculate the capacitance from the reactance  $X = \frac{1}{i\omega C}$  and  $C = \frac{-I_{amp}}{V_{amp}^2 \pi f \sin \delta}$  where

$I_{amp}$  is the current amplitude of the cell response and  $V_{amp}$  is the voltage amplitude of the applied voltage and  $f$  the used frequency. To resolve the response of the cell at low applied frequencies a high load resistance (e.g. 50 kOhm) was used with an RC time that is much shorter than the period time ( $1/f$ ) of the applied sine wave, i.e. it does not influence the cell response. In Figure 5c, the results obtained from Setup 2 are plotted due to the better measurement resolution at the low frequencies.

**Supplementary Note S1.** For simulating the cells with ions, we used the commercially available software SETFOS. SETFOS numerically solves a system of three coupled equations, namely the Poisson equation, the continuity equation, and the drift-diffusion equation. The Poisson equation is given by

$$\frac{\partial^2 \varphi(x)}{\partial x^2} = -\frac{q}{\epsilon}(p(x) - n(x) + c(x) - a(x) + N_D^+ - N_A^-) \quad (\text{S1})$$

where  $\varphi$  is the electrical potential,  $q$  is the charge of an electron,  $\epsilon$  is the absolute permittivity of the material,  $p(x)$  and  $n(x)$  are the hole and electron density respectively,  $a$  and  $c$  are the anion and cation concentration and  $N_D^+$  and  $N_A^-$  are the donor and the acceptor densities. The continuity equations for the electrons and holes are given by

$$\frac{\partial n}{\partial t} = -\frac{1}{q} \frac{\partial J_n}{\partial x} - R(x) + G(x) \quad (\text{S2a})$$

$$\frac{\partial p}{\partial t} = -\frac{1}{q} \frac{\partial J_p}{\partial x} - R(x) + G(x) \quad (\text{S2b})$$

where  $J_n$  and  $J_p$  are the electron and hole current densities, respectively,  $R(x)$  is the recombination rate and  $G(x)$  is the generation rate. The drift-diffusion equations are given by

$$J_n = qn(x)\mu_n \frac{\partial \varphi}{\partial x} + qD_n \frac{\partial n(x)}{\partial x} \quad (\text{S3a})$$

$$J_p = qp(x)\mu_p \frac{\partial \varphi}{\partial x} + qD_p \frac{\partial p(x)}{\partial x} \quad (\text{S3b})$$

where  $\mu_n$  and  $\mu_p$  are the mobilities of electrons and holes,  $D_n$  and  $D_p$  are the diffusion constants of electrons and holes. The continuity equation, as well as the drift-diffusion equation, also applies to mobile ions. The mobility and the diffusion constants are related via the Einstein relation

$$D = \mu k_B T / q \quad (\text{S4})$$

It is important to note, we assumed that mobile ions are only created in the bulk, although they may move throughout the whole device. Additionally, the same density of immobile anions is introduced in the bulk. The minority carrier concentration at equilibrium can then be calculated from these results using the following equation

$$n_0(x)p_0(x) = n_i^2 = N_C N_V \exp\left(\frac{-E_g}{k_B T}\right) \quad (\text{S5})$$

where  $n_i$  is the intrinsic carrier concentration and  $E_g$  the bandgap. The Recombination in the bulk material is given by the following equations

$$R(x) = R_{\text{SRH}} + R_{\text{radiative}} \quad (\text{S6a})$$

$$R_{\text{radiative}}(x) = k_2(n(x)p(x) - n_i^2) \quad (\text{S6b})$$

$$R_{\text{SRH}} = \frac{n(x)p(x) - n_i^2}{(n(x) + n_1)\tau_p + (p(x) + p_1)\tau_n} \quad (\text{S6c})$$

where  $k_2$  is the radiative radiation coefficient,  $\tau_p$  and  $\tau_n$  are the SRH-lifetimes for holes and electrons and  $n_1 = N_C \exp(-(E_C - E_T)/k_B T)$  and  $p_1 = N_V \exp((E_V - E_T)/k_B T)$  is the generation of electrons in the conduction band and holes in the valence band from the trap level, respectively. The minimum SRH lifetime in the bulk is given by

$$\tau_{p/n} = 1/(N_t v_{\text{th}} \sigma) \quad (\text{S7})$$

where  $N_t$  is the trap density in the bulk. The Generation is given by

$$G(x) = \int_{\lambda_{\min}}^{\lambda_{\max}} \alpha(\lambda) N_{\text{phot}}(\lambda, x) d\lambda \quad (\text{S8})$$

Where  $\alpha$  is the wavelength-dependent absorptivity, which we determined experimentally,  $N_{\text{phot}}$  is the photon flux at each position, which is calculated by using a Transfer Matrix Formalism.

**Supplementary Note S2.** According to Ravishankar et al. the step-like capacitance can be modeled by a series connection of three R | C-circuit, with three capacitances  $C_{\text{HF}} \ll C_{\text{IF}} \ll C_{\text{LF}}$  and the respective resistances  $R_{\text{HF}} \ll R_{\text{IF}} \ll R_{\text{LF}}$ .<sup>2</sup> The validity of this assumption will be discussed later. The subscripts refer to their characteristic frequency  $\omega = (RC)^{-1}$ . One can then calculate the frequency-dependent impedance and capacitance. Notably this recreates the step-like behaviour and the steps in capacitances can be quantified. Neglecting series resistances, this yields for  $\omega \gg \omega_{\text{IF}} \gg \omega_{\text{LF}}$ :

$$C = \left( \frac{1}{C_{\text{HF}}} + \frac{1}{C_{\text{IF}}} + \frac{1}{C_{\text{LF}}} \right)^{-1} \approx C_{\text{HF}} \quad (\text{S9})$$

For  $\omega_{\text{IF}} \gg \omega \gg \omega_{\text{LF}}$ :

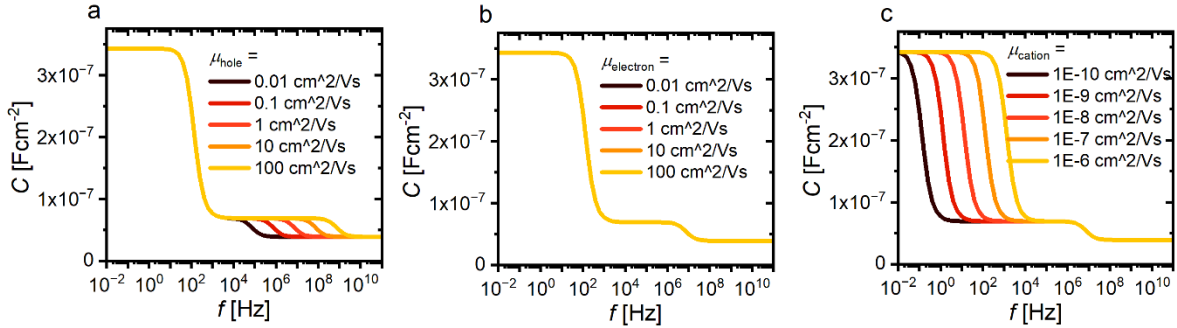
$$C = \left( \frac{(R_{\text{HF}} + R_{\text{IF}})^2}{R_{\text{HF}}^2 C_{\text{HF}} + R_{\text{IF}}^2 C_{\text{IF}}} + \frac{1}{C_{\text{LF}}} \right)^{-1} \approx C_{\text{IF}} \quad (\text{S10})$$

And for  $\omega_{\text{IF}} \gg \omega_{\text{LF}} \gg \omega$ :

$$C = \left( \frac{(R_{\text{HF}} + R_{\text{IF}} + R_{\text{LF}})^2}{R_{\text{HF}}^2 C_{\text{HF}} + R_{\text{IF}}^2 C_{\text{IF}} + R_{\text{LF}}^2 C_{\text{LF}}} \right)^{-1} \approx C_{\text{LF}} \quad (\text{S11})$$

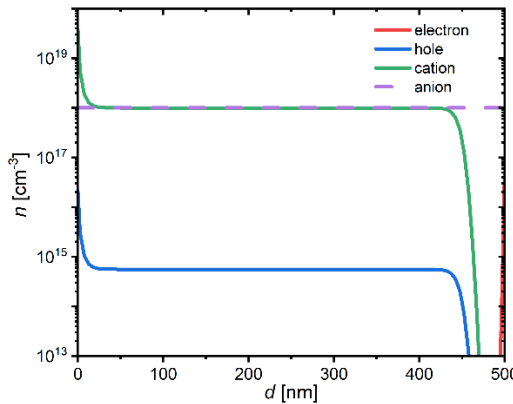
However, contrary to the reference,<sup>2</sup> we consider only the bulk and not additional transport layers. Therefore, any capacitances that are not part of the geometrical capacitance of the perovskite must originate from the formation of electrostatic layers. In order to investigate the origin these electrostatic layers, and therefore the capacitance steps, we vary the mobility of each charge carrier. As **Supplementary Figure S1** shows, the onset of the intermediate frequency is dependent on the hole mobility, while the onset of the low frequency step depends on the cation mobility. This is because the mobility is inversely proportional to the resistance, which is itself inversely proportional to the characteristic frequency. We can thus deduce that the  $C_{\text{IF}}$  and  $R_{\text{IF}}$  are linked to holes, while  $C_{\text{LF}}$  and  $R_{\text{LF}}$  are linked to mobile ions. Furthermore,  $C_{\text{HF}}$  is equal to  $C_{\text{geom}} = \epsilon \epsilon_0 d^{-1} = 3 \times 10^{-8} \text{ F cm}^{-2}$ . Since ions have the

lowest mobility of the charge carriers, their resistance is higher, justifying the earlier assumption that  $R_{\text{HF}} \ll R_{\text{IF}} \ll R_{\text{LF}}$ .



**Supplementary Figure S1** Varying the mobility of a charge carrier changes its characteristic frequency, which is visible through the onset of the related capacitance step. While **a)** there is a clear relationship between the hole mobility and the intermediate frequency onset in our simulation, **b)** the electron mobility has no impact. In contrast, **c)** the ion mobility shifts the low characteristic frequency, suggesting that the low frequency capacitance step is caused by an ionic electrostatic layer.

To fully understand the  $C$ - $f$ -curve it is important to investigate why the holes capacitive contribution is visible, whereas that of the electrons is not. **Supplementary Figure S2** shows the charge carrier density throughout the perovskite without TLs at  $V_{\text{app}} = 0$  V using an ionic density of  $10^{18} \text{ cm}^{-3}$ . Even though there is no illumination, the hole density is quite high even without doping. This might be because the mobile cation density in the bulk part of the perovskite (20 nm-450 nm) is lower than the immobile anion density, causing it to be slightly negatively charged and leading to the injection of holes. This difference between the hole and electron density amounts to  $5 \times 10^{14} \text{ cm}^{-3}$  in this case. The hole density distribution also reveals the formation of electrostatic layers, explaining the dependence on the hole mobility of the intermediate frequency step. Because the excess hole density is also influenced by the ion density,  $C_{\text{IF}}$  is indirectly related to the ionic density. This holds for both the  $C$ - $f$  as well as the Mott-Schottky measurement.



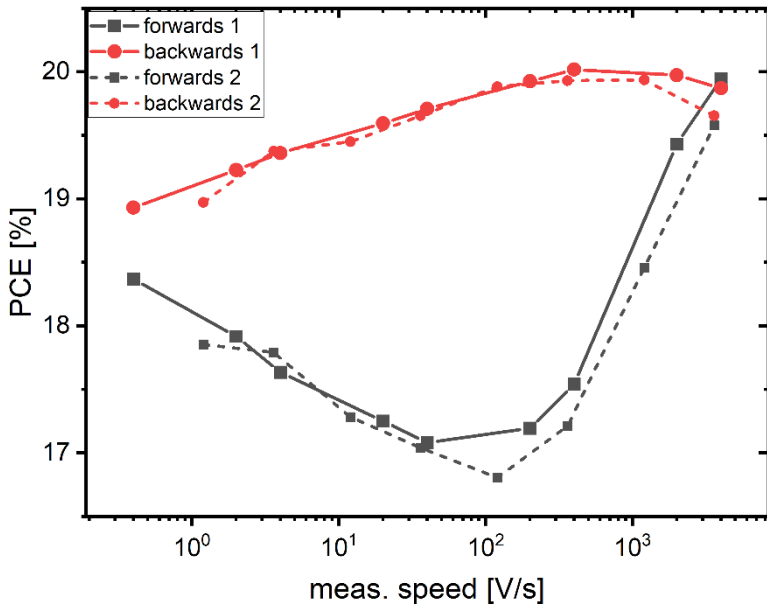
**Supplementary Figure S2** shows the charge carrier density throughout the perovskite without TLs at  $V_{\text{app}} = 0$  V using an ionic density of  $10^{18} \text{ cm}^{-3}$ . Due to a slight excess of immobile anions in the bulk part

of the perovskite, holes can be injected. These form electrostatic layers, which explains their influence on the capacitance measurements.

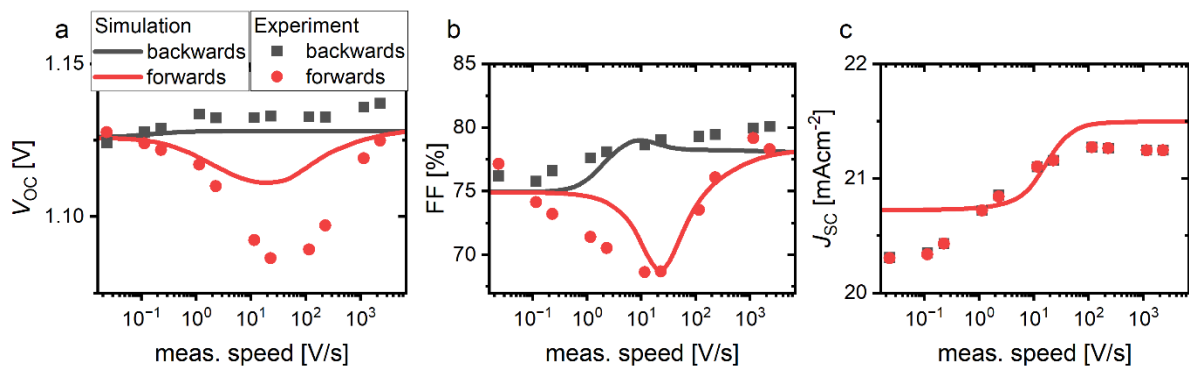
**Supplementary Table S1.** Simulation parameters for the standard cells. Most of the values are adapted from earlier studies<sup>3</sup>

Parameter	Symbol	Value	Unit
Majority carrier band offset between perovskite and ETL	$\Delta E_{\text{maj,c}}$	0	eV
Majority carrier band offset between perovskite and HTL	$\Delta E_{\text{maj,v}}$	0	eV
Lifetime in perovskite	$\tau_{\text{pero}}$	500	ns
Lifetime in HTL	$\tau_p$	1	ns
Lifetime in ETL	$\tau_n$	1	ns
Ionized acceptors in HTL	$N_{A,p}^-$	0	cm <sup>-3</sup>
Ionized donors in ETL	$N_{D,n}^+$	0	cm <sup>-3</sup>
Carrier recombination velocity from perovskite to the HTL	$S_{\text{HTL}}$	100	cm/s
Carrier recombination velocity from perovskite to the ETL	$S_p$	2000	cm/s
Thickness of PTAA	$d_{\text{HTL}}$	10	nm
Thickness of perovskite	$d_{\text{pero}}$	500	nm
Thickness of C <sub>60</sub>	$d_{\text{ETL}}$	30	nm
Offset between metal and PTAA	$\Delta E_{F,\text{metal}-p}$	0.1	eV
Offset between metal and C <sub>60</sub>	$\Delta E_{F,\text{metal}-n}$	0.1	eV
Device built-in voltage	$V_{\text{BI}}$	1.4	V
Bandgap PTAA	$E_{G,\text{HTL}}$	3.0	eV
Electron affinity PTAA	$E_{A,\text{HTL}}$	2.5	eV
Bandgap perovskite	$E_{G,\text{pero}}$	1.62	eV
Electron affinity perovskite	$E_{A,\text{pero}}$	3.9	eV
Electron affinity ETL	$E_{A,\text{ETL}}$	3.9	eV
Bandgap C <sub>60</sub>	$E_{G,\text{ETL}}$	2.0	eV
Electron mobility in C <sub>60</sub>	$\mu_{n,\text{ETL}}$	1x10 <sup>-2</sup>	cm <sup>2</sup> /Vs
Hole mobility in PTAA	$\mu_{p,\text{HTL}}$	1.5x10 <sup>-4</sup>	cm <sup>2</sup> /Vs
Electron mobility in perovskite	$\mu_{n,\text{pero}}$	1	cm <sup>2</sup> /Vs
Hole mobility in perovskite	$\mu_{p,\text{pero}}$	1	cm <sup>2</sup> /Vs
Relative dielectric constant PTAA	$\epsilon_{\text{HTL}}$	3.5	
Relative dielectric constant perovskite	$\epsilon_{\text{pero}}$	22	
relative dielectric constant C <sub>60</sub>	$\epsilon_{\text{ETL}}$	5.0	
Effective electron density of states in HTL	$N_{C/V,\text{HTL}}$	1x10 <sup>20</sup>	cm <sup>-3</sup>
Effective electron density of states in C <sub>60</sub>	$N_{C/V,\text{ETL}}$	1x10 <sup>20</sup>	cm <sup>-3</sup>

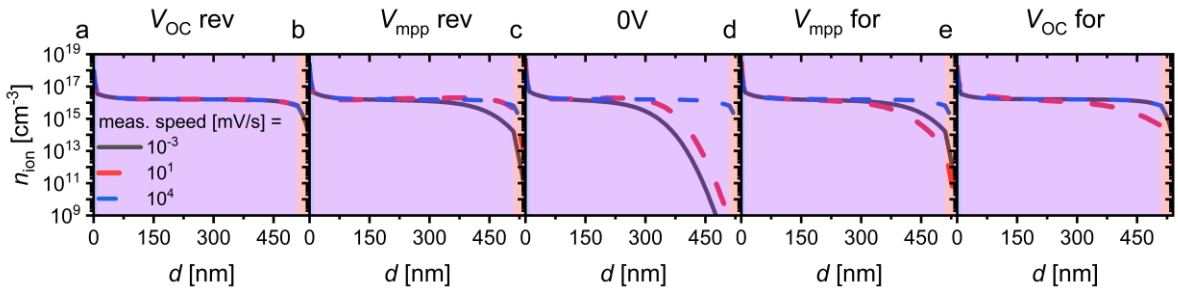
Effective electron density of states in perovskite	$N_{C/V,pero}$	$2.2 \times 10^{18}$	$\text{cm}^{-3}$
Ion density	$n_{\text{ion}}$	$2 \times 10^{16}$	$\text{cm}^{-3}$
Ion mobility	$\mu_{\text{ion}}$	$10^{-7}\text{--}10^{-8}$	$\text{cm}^2/\text{Vs}$



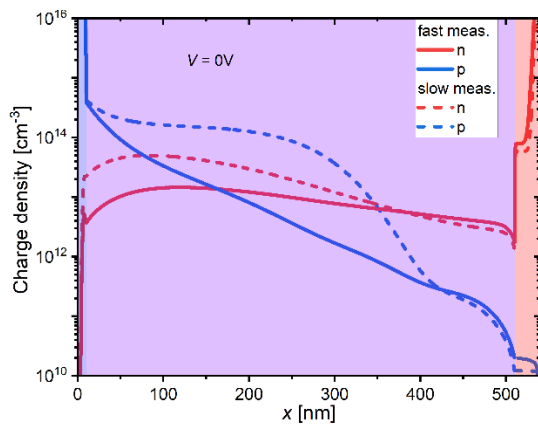
**Supplementary Figure S3.** Experimentally obtained fast hysteresis plot. There is no significant difference between the two back to back measurements on the same cell. However, degradation may significantly alter the hysteresis, for example due to an aging-induced influx of mobile ions or interfacial degradation.



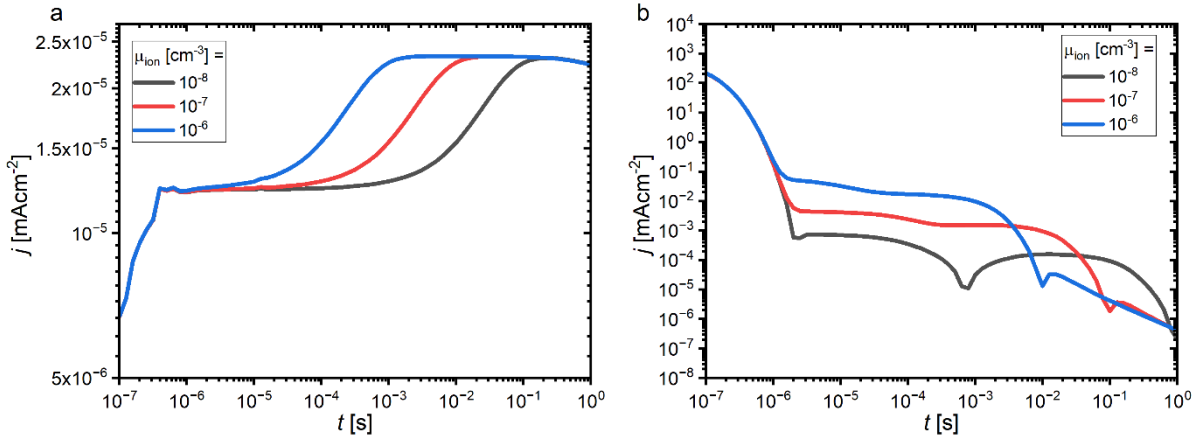
**Supplementary Figure S4.** A comparison of experimental and simulated hysteresis of the JV performance metric parameters, a)  $V_{\text{OC}}$ , b) FF and c)  $J_{\text{SC}}$ . Panel a) shows that a loss of  $V_{\text{OC}}$  occurs at medium scan speed in the forward direction, thereby contributing to the hysteresis. However, the difference between the  $V_{\text{OC}}$  at fast and slow scan speeds, i.e. the loss due to ion movement is small in this cell. This is because the prebias was chosen to be similar to the  $V_{\text{OC}}$ , which results in a nearly homogenous distribution of ions. In the case of the fill factor, panel b) a large hysteresis occurs at medium scan speeds. Finally, in the case of the  $J_{\text{SC}}$ , panel c), there is no hysteresis is visible here since there is only one measurement point at 0 V applied voltage. However, there is a significant difference between the slow and fast scan speed, which dominates the ion induced PCE losses. Notably, all effects are reproduced by the simulations, although the absolute values vary slightly.



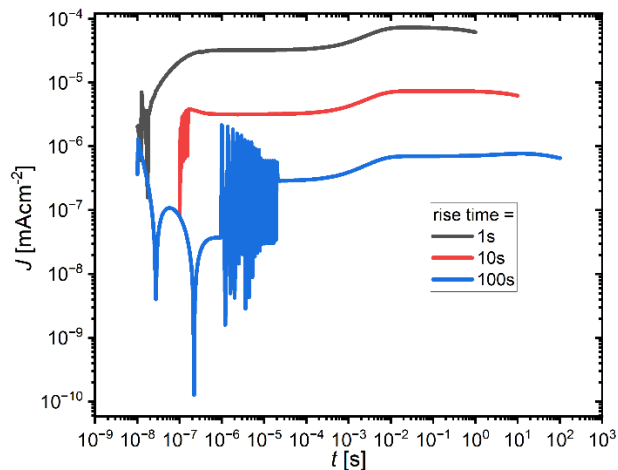
**Supplementary Figure S5** shows the cation density distribution in the cell for a slow, medium, and fast scan speed at different characteristic voltage points. **a)** shows the initial ion distribution for the JV measurement at  $V_{OC}$ . As the cell is preconditioned at this voltage point for all the scanning speeds, there is no difference between the curves. As voltage is ramped down to  $V_{mpp}$  **b)** at slow scan speed, a noticeable quantity of cations has already moved from the right side of the bulk and the ETL towards the HTL-side. At short-circuit-condition **c**), the slowest measurement shows the most notable shift towards the HTL-side and, therefore, the most significant screening effect. This correlation explains why the  $J_{sc}$  increases monotonously with increasing scanning speed. However, this is not the case for the forward FF scan, as shown in **d**). At medium scan speed, the ions lag behind the applied voltage. Hence, the ionic distribution has not changed as much from short-circuit conditions compared to the slow measurement speed. Consequently, the screening effect is less prominent at  $V_{mpp}$  for the slow scan speed case, resulting in a minimum in FF in forward direction at intermediate scan speeds. The same can be said for the forward voltage ramp at  $V_{OC}$  **e**), where the ion distribution is the same as the initial one for the slow scan speed. This contrasts with the more significant ionic accumulation for medium scan speeds, explaining the minimum in forwards  $V_{OC}$ .



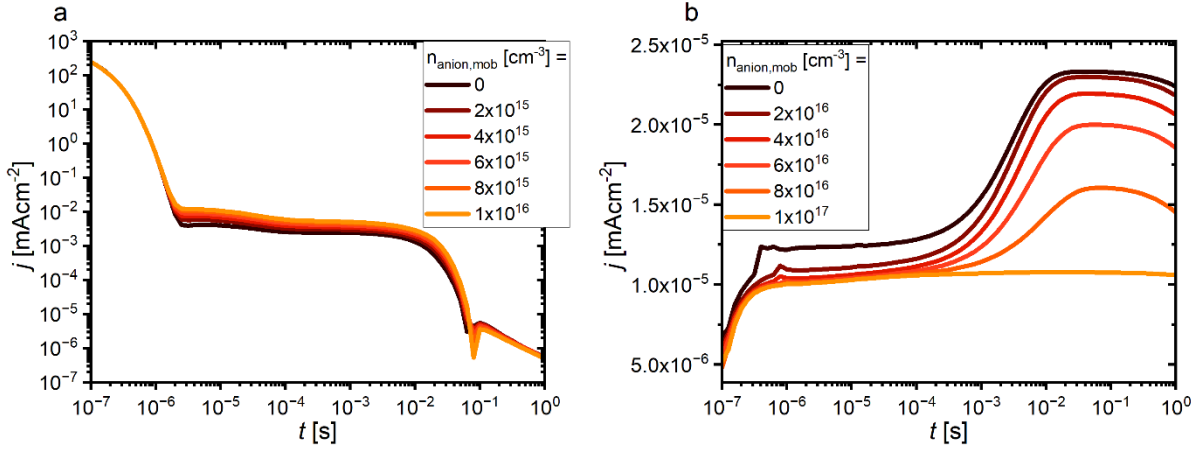
**Supplementary Figure S6** Simulated electron and hole density distribution at short-circuit conditions for the fast ( $10^4$  mV/s) and slow measurement ( $10^{-3}$  mV/s). Both electron and hole carrier densities are higher in the bulk. Moreover, the electron density at the HTL-side is significantly higher during the slow measurement than during the fast measurement. Therefore, the recombination is not only increased in the bulk but also at the HTL-side and thus the recombination velocity at this interface is critical for  $J_{sc}$  loss (in case of dominant halide vacancies). The reason for the electron accumulation at the HTL-side at 0 V is the accumulation of the cations, causing the potential to almost flatten out at this side, whereas there is still a significant driving field at the ETL-side, which prevents hole accumulation.



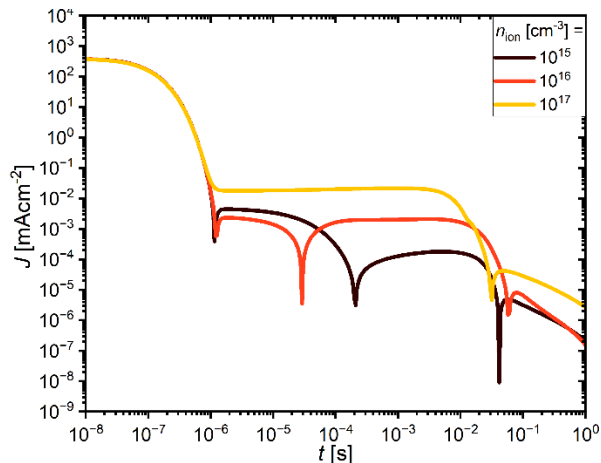
**Supplementary Figure S7.** **a)** Simulated CELIV transients for  $n_{ion} = 10^{17} \text{ cm}^{-3}$  and various ion mobilities. Increasing the mobility by one order of magnitude shifts the ionic bump by one order of magnitude to earlier times as expected. **b)** Simulated BACE transients for  $n_{ion} = 10^{16} \text{ cm}^{-3}$  and various ion mobilities. Increasing the mobility increases the current during the ionic plateau but leads to an earlier end of said plateau as is expected for TOF. Calculating the ionic density for the three curves yields a maximal difference of  $4 \times 10^{14} \text{ cm}^{-3}$ , which is small compared to the input ionic density.



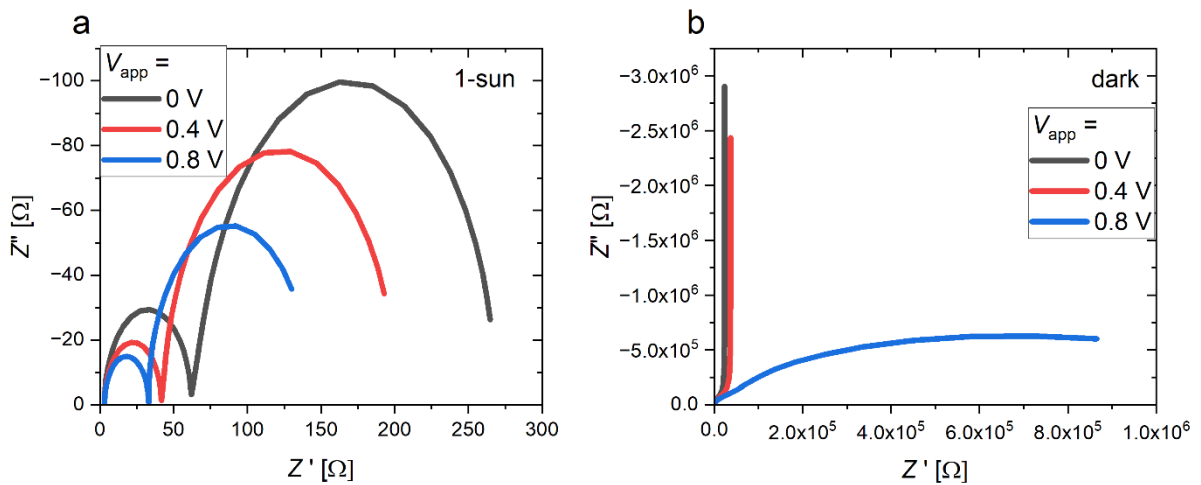
**Supplementary Figure S8.** Simulated current for CELIV measurements with different rise times and  $n_{ion} = 10^{17} \text{ cm}^{-3}$  and  $V_{ext} = 1 \text{ V}$ . Notably, the simulations show large fluctuations in the nanosecond to microsecond timescale due to low voltage ramp rates and the resulting low currents. Importantly, it is very challenging, even in the simulations, to fully resolve the ionic bump at high ion densities  $> \text{CU/ed}$  and long rise times. This is because lowering the ramp rate to resolve longer timescales slows the extraction and reduces the measured current. This might be circumvented in principle by higher maximum reverse voltages, which will however easily break the cell in the experiment.



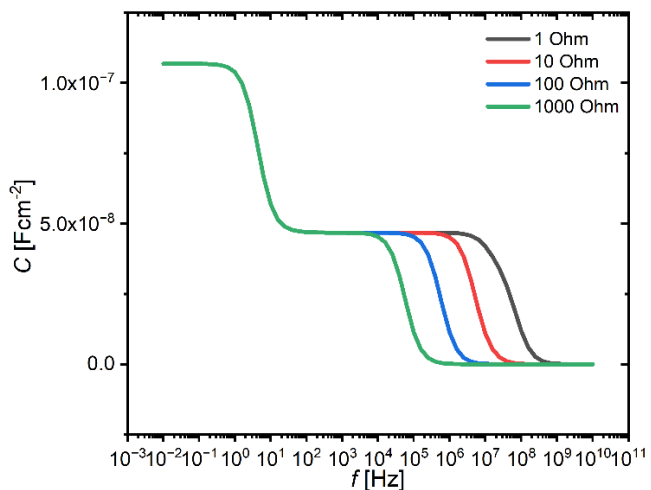
**Supplementary Figure S9.** **a)** Simulated BACE currents for mobile cation densities of  $10^{16}$  cm<sup>-3</sup> with various mobile anion densities. A preconditioning voltage of 1.5 V and an extraction voltage of 0 V was used. Increasing the mobile anion density from 0 (standard) up to the density of mobile cation increases the current during the ion-dominated plateau due to the additional anion current. **b)** Simulated CELIV currents for mobile cation densities of  $10^{17}$  cm<sup>-3</sup> with various mobile anion densities. A preconditioning voltage of 0 V and an extraction voltage of -0.4 V was used. The ionic bump actually decreases upon the implementation of mobile anions to the point that the bump vanishes at equal mobile ion densities. Therefore, like the capacitance measurements, CELIV is sensitive to the excess mobile ion density of one species in the presented case. The fact that we observe an ionic bump experimentally is consistent with the hypothesis that mobile vacancies dominate over mobile interstitials. The difference between the two techniques in this regard might be related to the voltage-dependence of the accumulation layer. As shown in Figure 2d), the accumulation layer barely changes between a prebias of 0 V and -1 V, while a large difference is visible at prebiases near the  $V_{bi}$ . In the case of two oppositely charged mobile ion species with the same density, there is an accumulation layer at either side of the device, but there is no depletion layer. Therefore, a noticeable difference between the initial and final cation distribution during the CELIV scan, and therefore a noticeable ionic drift, only occurs when preconditioning close to the  $V_{bi}$ , which is the case for the BACE simulation but not the CELIV simulation.



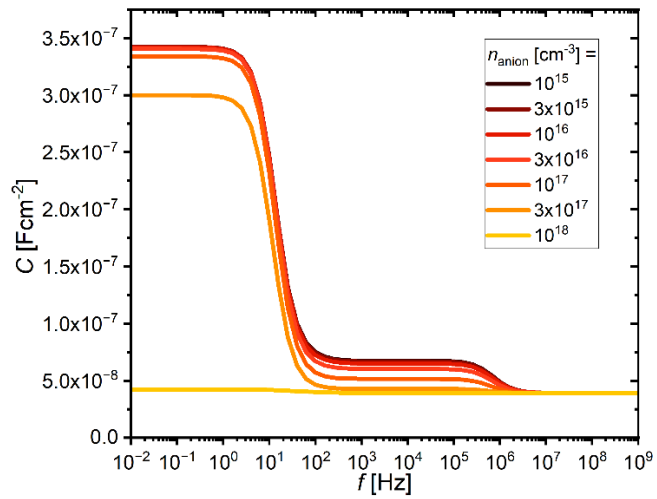
**Supplementary Figure S10** Simulated CELIV transients for various ionic densities with prebias at  $V_{bi}$ . The voltage is ramped down rapidly to 0 V and then gradually to -1 V. While this measurement can work in principle, the transients are nearly identical to BACE, thus making the ramp unnecessary.



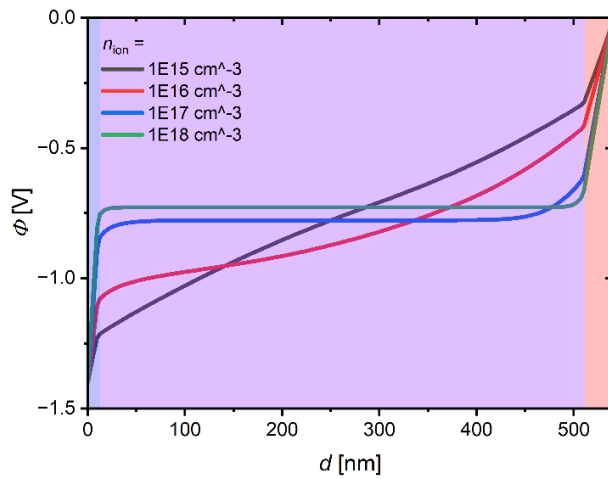
**Supplementary Figure S11.** Simulated Nyquist plots using the model in Figure 4 and  $n_{ion} = 2 \times 10^{16} \text{ cm}^{-3}$  **a)** under 1-sun illumination and **b)** in the dark. Frequencies from 1 Hz to  $10^8$  Hz were used.



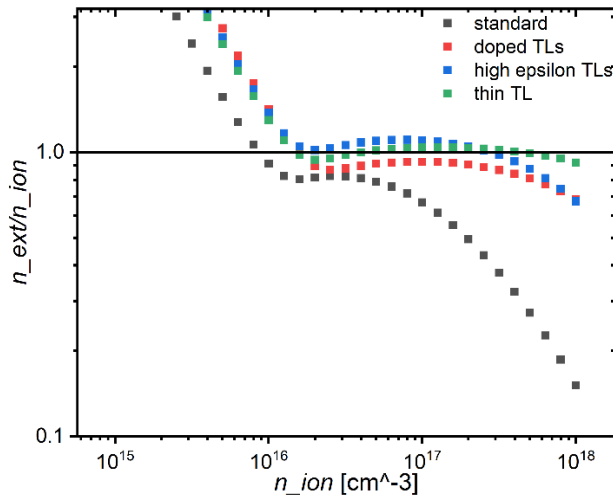
**Supplementary Figure S12.** Simulated capacitance vs. frequency curve with  $n_{ion} = 10^{17} \text{ cm}^{-3}$  for various series (or load) resistances. While the low frequencies remain unchanged, the series resistance lowers the capacitance at high frequencies. Higher series resistances will lead to a downturn of the capacitance at lower frequencies as compared to lower series/load resistances.



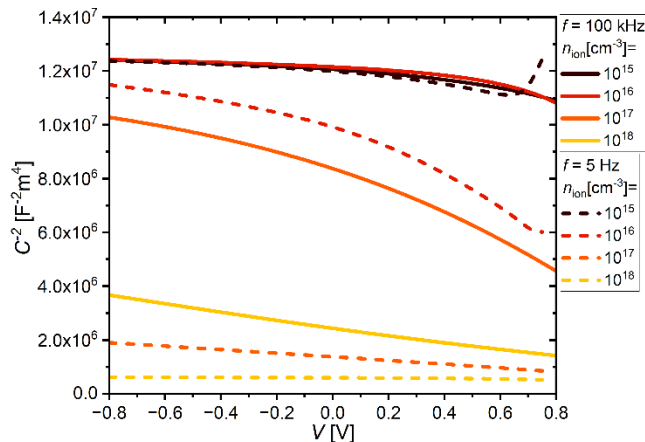
**Supplementary Figure S13.** *C-f-curves with a constant cation density of  $10^{18} \text{ cm}^{-3}$  and various anion densities. Both the intermediate and low frequency plateaus drop with increasing anion density, vanishing at equal ion density. This capacitive method is therefore only sensitive to an excess of 1 mobile ions species.*



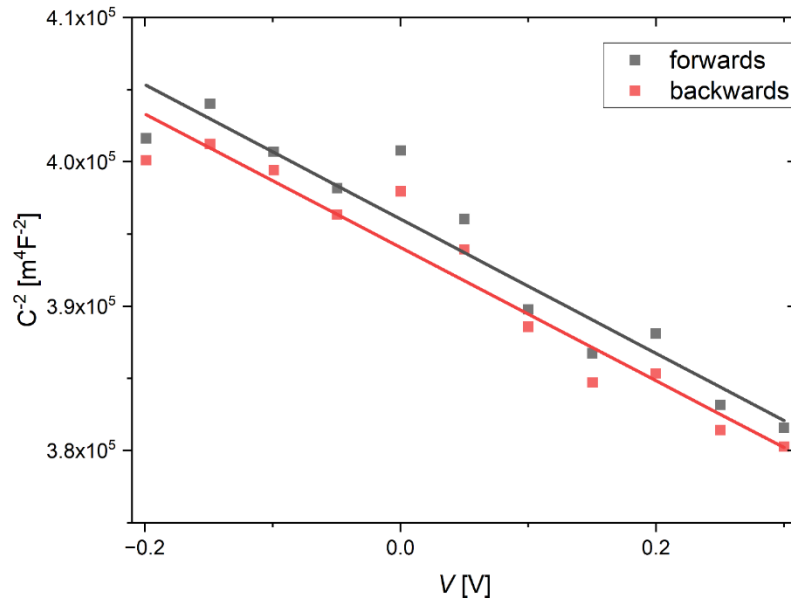
**Supplementary Figure S14.** *Simulated potential drop across the cell stack at various mobile ion densities. The field will mostly drop (linearly) across the perovskite layer for low ionic densities. At high ion densities, the perovskite is almost field-free since the potential drops across the transport layers.*



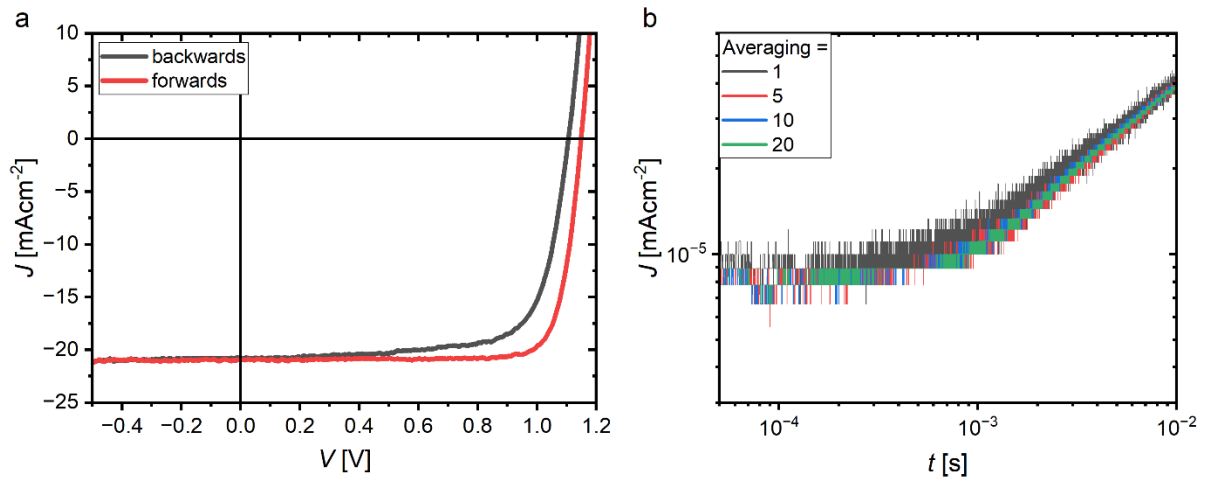
**Supplementary Figure S15** shows the simulated calculated ion density compared to the input ion density when using eq. 5 and measuring low-frequency capacitance. In principle, multiple measures can be taken to reduce the field drop across the TLs, producing more accurate ionic density results, however this is difficult to realize experimentally.



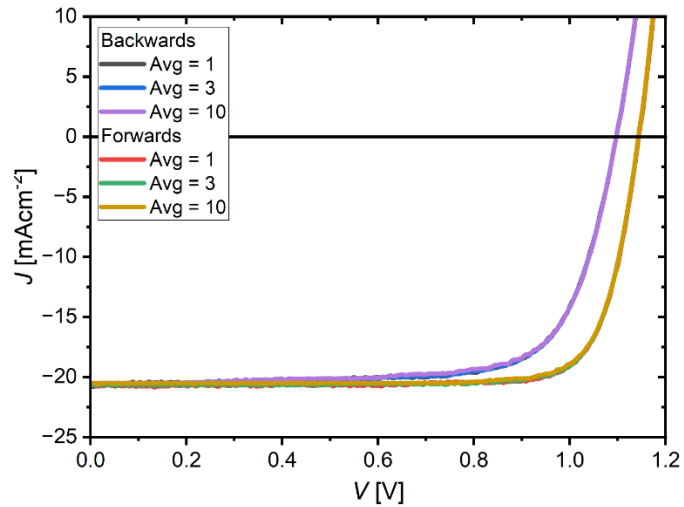
**Supplementary Figure S16.** Simulated Mott-Schottky plots for intermediate and low frequencies reveal stark differences because of the different layers probed at that frequency. Intermediate-frequency Mott-Schottky is nevertheless sensitive to changes in the ionic density because ion redistribution modifies the field, which causes a redistribution of electronic charges and an influx of holes (**Supplementary Note S2**). At intermediate frequencies, the capacitive influence of electron holes due to the formation of electrostatic layers can be measured.



**Supplementary Figure S17.** Low frequency Mott-Schottky measurement for a partly degraded cell. The slope is unaffected by the measurement direction due to the low scan speed of  $\sim 3 \times 10^{-3}$  V/s.



**Supplementary Figure S18.** a) Experimentally obtained fast hysteresis JV measurement showing stable current for reverse currents up to -0.5V. b) Experimentally obtained CELIV measurement show negligible influence of the averaging count onto the transient and therefore onto the integral



**Supplementary Figure S19.** Experimentally obtained JV curves showing no dependence of averaging count on current transient

## References

- (1) Le Corre, V. M.; Diekmann, J.; Peña-Camargo, F.; Thiesbrummel, J.; Tokmoldin, N.; Gutierrez-Partida, E.; Peters, K. P.; Perdigón-Toro, L.; Futscher, M. H.; Lang, F.; Warby, J.; Snaith, H. J.; Neher, D.; Stolterfoht, M. Quantification of Efficiency Losses Due to Mobile Ions in Perovskite Solar Cells via Fast Hysteresis Measurements. *Sol. RRL* **2022**, *6* (4), 2100772.  
<https://doi.org/10.1002/SOLR.202100772>.
- (2) Ravishankar, S.; Liu, Z.; Rau, U.; Kirchartz, T. Multilayer Capacitances: How Selective Contacts Affect Capacitance Measurements of Perovskite Solar Cells. *PRX Energy* **2022**, *1* (1), 013003.  
<https://doi.org/10.1103/prxenergy.1.013003>.
- (3) Diekmann, J.; Caprioglio, P.; Futscher, M. H.; Le Corre, V. M.; Reichert, S.; Jaiser, F.; Arvind, M.; Toro, L. P.; Gutierrez-Partida, E.; Peña-Camargo, F.; Deibel, C.; Ehrler, B.; Unold, T.; Kirchartz, T.; Neher, D.; Stolterfoht, M. Pathways toward 30% Efficient Single-Junction Perovskite Solar Cells and the Role of Mobile Ions. *Sol. RRL* **2021**, *5* (8).  
<https://doi.org/10.1002/solr.202100219>.